



Castro, J. M., de Gea, G. A., Quijano, M. L. L., Aguado, R., Froehner, S., Naafs, B. D. A., & Pancost, R. D. (2019). Complex and protracted environmental and ecological perturbations during OAE 1a: Evidence from an expanded pelagic section from south Spain (Western Tethys). *Global and Planetary Change*, 183, [103030].
<https://doi.org/10.1016/j.gloplacha.2019.103030>

Peer reviewed version

License (if available):
CC BY-NC-ND

Link to published version (if available):
[10.1016/j.gloplacha.2019.103030](https://doi.org/10.1016/j.gloplacha.2019.103030)

[Link to publication record in Explore Bristol Research](#)
PDF-document

This is the author accepted manuscript (AAM). The final published version (version of record) is available online via Elsevier at <https://www.sciencedirect.com/science/article/pii/S0921818119301730?via%3Dihub>. Please refer to any applicable terms of use of the publisher.

University of Bristol - Explore Bristol Research

General rights

This document is made available in accordance with publisher policies. Please cite only the published version using the reference above. Full terms of use are available:
<http://www.bristol.ac.uk/red/research-policy/pure/user-guides/ebr-terms/>

31 main feature during OAE 1a in the western Tethys with notable changes extending from the onset to the post-OAE 1a
32 interval.

33

34 **KEYWORDS:**

35 Oceanic anoxic event 1a, Aptian, Biomarkers, Trace Elements, Environmental perturbations

36

37 **1. Introduction**

38 Oceanic anoxic events (OAEs) represent marked changes in the state of the Earth System (Jenkyns, 2010), linked to major
39 perturbations of the global carbon cycle that influenced both the marine and terrestrial realm (Skelton, 2003; Hay, 2017;
40 Xu et al., 2017). The main sedimentary feature of OAEs is the deposition of widespread marine organic rich sediments
41 (Schlanger and Jenkyns, 1976), although this deposition is not strictly synchronous (Jenkyns, 2010). OAEs have been
42 considered as hyperthermal or hothouse episodes (Jenkyns, 2010, 2018; Kidder and Worsley, 2010; Foster et al., 2018),
43 which are interpreted as geologically abrupt events of increased atmospheric CO₂, global warming, a C-isotope excursion
44 and reduction in oceanic oxygen content, among their main features. High-resolution studies on the isotopic signature of
45 OAEs have demonstrated that C-isotope stratigraphy, when combined with biostratigraphy, provides a robust correlation
46 tool (Menegatti et al., 1998). OAEs are typically characterized by $\delta^{13}\text{C}$ anomalies, interpreted as the result of light carbon
47 input and widespread deposition of organic matter and subsequent ¹²C drawdown (e.g., Jarvis et al., 2011; Jenkyns, 2010).

48 The Early Aptian OAE 1a is one of the largest and is linked to environmental, biotic and sedimentary changes, that
49 affected both marine and continental environments (e.g., Föllmi, 2012; Robinson et al., 2017). A distinctive feature of OAE
50 1a is the presence of a negative $\delta^{13}\text{C}$ excursion preceding the main positive isotope excursion (Menegatti et al., 1998). One
51 of the first C-isotope stratigraphies of OAE 1a was based on the study of the Cismon and Rotter Sattel sections from the
52 Alpine Tethys, leading to the definition of eight carbon segments (C1 to C8, Menegatti et al., 1998). These segments have
53 been established as a standard for the early Aptian C-isotope stratigraphy and are used for stratigraphic correlation in
54 sections worldwide; in the Tethys domain (Menegatti et al., 1998; Hochuli et al., 1999; Luciani et al., 2001; de Gea et al.,
55 2003; Erba and Tremolada, 2004; Heimhofer et al., 2004; Aguado et al., 2008, 2014a, b; Li et al., 2008; de Gea et al., 2008b;
56 Mehay et al., 2009; Millán et al., 2011, 2014; Najarro et al., 2011; Stein et al., 2011; Sánchez-Hernández and Maurrasse,
57 2016), in the Boreal domain (Gröcke et al., 1999; Föllmi et al., 2006; Mutterlose and Bottini, 2013), in the Pacific (Jenkyns,
58 1995; Ando et al., 2002; Price, 2003; Dumitrescu and Brassell, 2005), and Mexico (Bralower et al., 1999; Nuñez-Useche et
59 al., 2015).

60 OAE 1a was originally defined as the interval C4 to the base of C7 (Menegatti et al., 1998). Recently most studies
61 (e.g., Erba et al., 1999, 2010; Malinverno et al., 2010; Heldt et al., 2012; Aguado et al., 2014a, b; Mutterlose et al., 2014;
62 Bottini et al., 2015; Naafs et al., 2016; Jenkyns, 2018) place the onset of the OAE 1a at the base of the negative shift
63 (segment C3), where the first organic-rich black shales and first evidence of environmental change are recorded.

64 The most accepted trigger for OAE 1a is increased atmospheric CO₂ concentrations, derived from volcanogenic
65 and/or methanogenic sources (e.g., Weissert and Erba, 2004; Mehay et al., 2009; Bottini et al., 2012; Erba et al., 2010,
66 2015; Naafs et al., 2016). Additionally, the intrusion of magma into organic-rich sediments has been also considered a
67 source of CO₂ (Polteau et al., 2016). OAE 1a may have been triggered by the emplacement of the Ontong Java Plateau in
68 the central Pacific Ocean (e.g., Erba, 1994; Larson and Erba, 1999; Jones and Jenkyns, 2001; Jenkyns, 2010). Perturbations
69 in the Os isotope record (Tejada et al., 2009; Bottini et al., 2012) and *p*CO₂ reconstructions based on biomarkers (Méhay
70 et al., 2009; Naafs et al., 2016) are consistent with C-input from such (submarine) volcanism during the onset of OAE 1a. A
71 release of isotopically light carbon from partial methane hydrate dissociation might have played a minor role in the OAE1a
72 (Méhay et al., 2009), and was likely not a major source of *p*CO₂ during OAE 1a (Naafs et al., 2016).

73 Elevated *p*CO₂ led to global warming (Beerling and Rogers, 2002; Ando et al. 2008; Tejada et al., 2009; Mehay et
74 al., 2009; Mutterlose et al., 2014; Bottini et al., 2015; Naafs and Pancost, 2016) and a subsequent activation of the
75 hydrological cycle, causing an increased nutrient influx to the ocean due to higher weathering rates (Kump et al., 2000;
76 Jenkyns, 2010; Blättler et al., 2011). Many studies have documented an increase in surface-water fertility accompanied by
77 high primary productivity (e.g., Aguado et al., 2014a; Bottini et al., 2015). The key feature of the sedimentary record of
78 OAE 1a, and OAEs in general, is the widespread accumulation of organic-rich marine deposits (e.g. Jenkyns, 2010).
79 Extensive accumulation of organic matter in marine environments has been classically linked to enhanced productivity
80 and/or enhanced preservation, being the last related to low oxygen concentrations (Demaison and Moore, 1980; Pedersen
81 and Calvert, 1990; Tyson, 2001, 2005). The discussion about the relative roles of both factors has been the origin of
82 controversies, with the balance now tipping in favor of the productivity as generally the more important factor during OAEs
83 (Jenkyns, 2010; Westermann et al., 2013; Aguado et al., 2014), although a combination of both origins is not mutually
84 exclusive. As plankton productivity increases the oxygen-minimum zone intensifies, in a positive feedback mechanism
85 (Jenkyns 2003). Other carbon-rich sediments, as sapropels (e.g., Martínez-Ruiz et al., 2015) are similarly explained.
86 Evidence from multiple independent organic and inorganic proxies is crucial to shed light into this controversy, and is the
87 aim of this study.

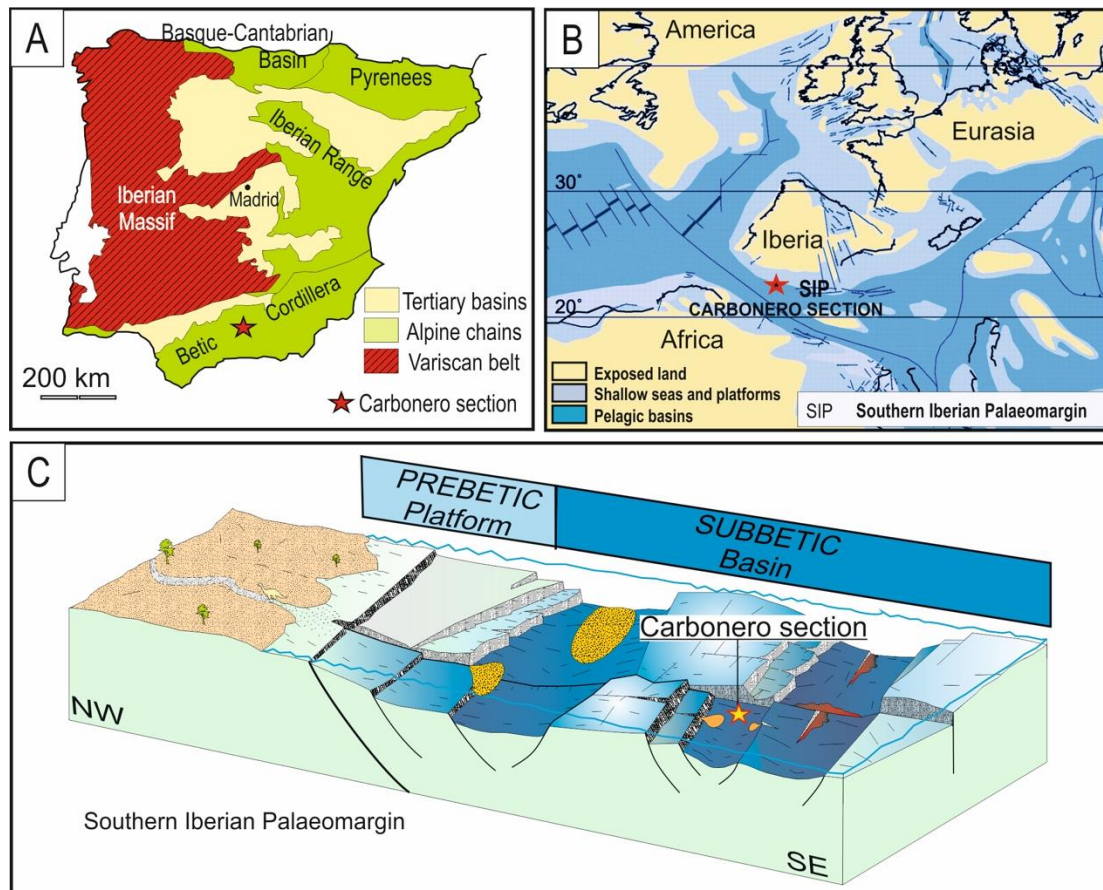
88 Detailed high-resolution studies show that, besides the general long-term environmental perturbations across
89 OAE 1a, rapid changes also occurred, pointing to a complex evolution during this event, with variations in redox conditions
90 (e.g., Westermann et al., 2013) or in temperatures (e.g., Dumitrescu et al 2006; Bottini et al., 2015; Naafs and Pancost,
91 2016; Jenkyns 2018). In this context, new high-resolution records enhancing the database of stratigraphy,
92 chemostratigraphy and biostratigraphy are crucial to establish the time and cause-effect relationships between the long
93 and short-term environmental changes, their causes and feedbacks, and the consequences in the biota. These will
94 contribute to unravelling the complex processes involved in this global perturbation of the carbon cycle, ultimately
95 increasing our understanding on the dynamics of Earth's system in a greenhouse world (Hay, 2017).

96 Here we document an expanded pelagic succession from the western Tethys, the Carbonero section in S. Spain.
97 We use high-resolution C-isotope stratigraphy and a combination of elemental and organic geochemistry to explore
98 changes in environmental conditions at this site and their impact in the biota. The aim of this study is to present a high-
99 resolution record of the early Aptian OAE 1a, adding a new correlation section to the global database. We also provide a
100 new detailed reconstruction of the environmental changes recorded in a western Tethys pelagic basin across OAE 1a,
101 allowing us to explore further aspects of local vs. global change in productivity and anoxia, and their impact on marine
102 ecosystems. This study aims to contribute to the knowledge of the functioning of the Earth System during hyperthermals,
103 which has a further interest as they are considered as analogues to present and future climate change.

104

105 **2. Location and geological background**

106 The Carbonero section is located in the Jaén province, Southeast Spain, in the site named Solana de Morales (geographic
107 coordinates: base, 37° 33' 39.40"N, 3° 48' 2.27"W; top, 37° 33' 41.85"N, 3° 48' 4.08"W) (Fig. 1A). This section belongs to
108 the Subbetic Zone of the External Zones of the Betic Cordillera (EZBCs), which comprises sedimentary successions
109 deposited in the South Iberian Palaeomargin (SIP) during the Alpine tectonic cycle (Triassic to the early Miocene, see Fig.
110 1B). The Lower Cretaceous sequence of the SIP includes thick successions (> 3000 m) of carbonates and siliciclastics that
111 were deposited on shallow platforms (mostly in the so-called Prebetic Zone, Fig. 1C) and hemipelagic/pelagic settings
112 (dominant in the Subbetic Zone, Fig. 1C) (e.g., Ruiz-Ortiz, 1980; Martín-Chivelet et al., 2002; Vera, 2004). At present, the
113 Subbetic is a major tectonic unit of the EZBCs, composed of several thrusts with a general SW–NE strike, made of mostly
114 Mesozoic pelagic successions. The Subbetic Zone is an allochthonous tectonic unit that thrusts over the Prebetic Zone, a
115 para-autochthonous unit made of shallow-marine sedimentary successions with intercalations of continental facies, that
116 represents the northern part of the EZBCs.



117

118 FIGURE. 1. A. Current location of the Carbonero section in the central part of the Betic Cordillera, southern Spain. B. Early
 119 Aptian (~120 Ma) palaeogeographic reconstruction of the western Tethys (simplified from Masse et al., 2000) showing the
 120 location of the Carbonero section in the Southern Iberian Palaeomargin (SIP). C. Reconstruction of the SIP during the Early
 121 Aptian (modified from de Gea et al., 2008b).

122

123 *2.1. Palaeogeography and palaeoclimates*

124 During the Early Cretaceous, the Carbonero section was located in the northwestern corner of the Tethys (Fig. 1B). The
 125 configuration of the SIP was defined by a series of basin-scale troughs and swells, bounded by large extensional faults
 126 roughly parallel to the continental margin, that were initiated in the Middle Jurassic (Fig. 1C) (e.g., Azéma et al., 1979;
 127 García Hernández et al., 1980; Vera, 1988; Ruiz-Ortiz et al., 2001). This tectonic pattern controlled strong lateral changes
 128 in subsidence, deposition rates and facies. During the Aptian, the SIP was strongly influenced by the relative motions of
 129 the contiguous Eurasian and African plates (Fig. 1B). Initiation of the seafloor spreading in the North Atlantic that started
 130 very early in the Cretaceous, led to a reversion in the sinistral movement between Iberia and Africa that had prevailed
 131 during part of the Jurassic (Ziegler, 1988). It started a phase of anti- clockwise rotation of Iberia relative to Europe, linked

132 to the opening of the Bay of Biscay from the middle Aptian onwards (Olivet, 1996; Vergès and García-Senz, 2001). In that
133 geodynamic framework, extensional tectonics prevailed in the SIP.

134 The onset of the Aptian was marked by a pulse in extensional tectonics, triggering the formation of tilted blocks
135 that resulted in notable lateral changes in subsidence rates, with highly subsident sectors surrounded by low subsident
136 and even uplifting sectors, controlled by listric faults (e.g., Martín-Chivelet et al., 2002; Vilas et al., 2003; Vera, 2004). De
137 Gea et al. (2008a) provided a detailed study of several sections within the area and proposed a model of a small subsiding
138 pelagic sub-basin bounded by active faults leading to scarps feeding the turbidite levels, associated with volcanic activity
139 (Fig. 1C). This small sub-basin has a thicker and more complete stratigraphic record than the surrounding areas, specifically
140 during the early Aptian, (Molina, 1987; Aguado et al., 1993; Molina and Hernández-Molina, 1993; de Gea et al., 2008). A
141 palaeolatitude of 20°–25° N has been inferred from the Aptian position of the section (e.g., Masse et al., 1993) (Fig. 1B).
142 According to the palaeoclimatic reconstructions of Chumakov et al. (1995), during the Aptian, the studied section was
143 located in the northern part of the equatorial arid belt, close to the boundary with the mid-latitude warm humid belt.
144 Palaeoclimatic reconstructions from a nearby section (La Frontera section, Aguado et al., 2014a), show interesting changes
145 towards more humid conditions across OAE 1a that could be explained by a southward expansion of the humid climate
146 belt during the early Aptian.

147

148 *2.2. Stratigraphy, sedimentology and biostratigraphy*

149 The stratigraphic succession of the Carbonero section mainly belongs to the Carbonero Formation (Molina, 1987) within
150 the Ventisquero-Sierra del Trigo tectonic unit (Sanz de Galdeano, 1973). The Carbonero Formation lies on the marly
151 limestones and grey marlstones (Berriasian–Barremian) of the Carretero Formation (de Gea, 2004; de Gea et al., 2008b).
152 Its top is not preserved due to faulting or localized erosion. The Carbonero Formation represents one of the most complete
153 records of Aptian sedimentation in the External Zones of the Betic Cordillera (de Gea et al., 2008b), which laterally
154 correlates with large hiatuses throughout the Subbetic Zone (Vera, 2004). Detailed stratigraphic and sedimentological
155 characterizations of this formation can be found in Molina (1987), Molina et al. (2001), de Gea (2004) and de Gea et al.
156 (2008b).

157 The Carbonero section (Fig. 2) was originally proposed as the stratotype of the Carbonero Formation (Molina, 1987),
158 and the present study focuses on the interval equivalent to its lower ~82 m. Three members, designated as lower, middle
159 and upper, were initially distinguished. The lower member (~18 m thick) lies on an unconformity at the top of the
160 marlstones and marly limestones of the Carretero Formation, and comprises a pebbly mudstone at the base, overlaid by

161 bluish-grey marlstones with several intercalations of calcareous turbidites and some barite concretions. The middle
162 member has a thickness of ~46 m and is composed of marlstones, black shales, dark clayey marlstones, and dark brown
163 radiolarite beds interbedded with dark siliceous shales. Some levels of fine-grained volcanoclastic rocks (cinerites) are
164 intercalated within the dark marlstones at about 30–32 m (Fig. 2). Two horizons of carbonate concretions are present at
165 ~45 m and ~51.5 m. The studied part of the upper member is ~16 m thick and comprises an alternation of light-green
166 marlstones and calcarenites. Previous studies (de Gea et al., 2008a, b, c; O’Dogherty et al., 2011; Quijano et al., 2012;
167 Aguado et al., 2014a, b) indicate that most of the sedimentary record of the middle member of the Carbonero formation
168 represents the local expression of the OAE 1a.

169 Biostratigraphic analysis of the Carbonero section is based mainly on calcareous nannofossils (Aguado et al., 1993;
170 Aguado, 1994; de Gea, 2004; de Gea et al., 2008a, c) although some radiolarian data also exist (Aguado et al., 1993;
171 O’Dogherty, 1994). Contrary to other outcrops of the Carbonero Formation (Aguado et al., 2014a, b), calcareous
172 microfossils at Solana de Morales are only moderately preserved or absent. Moderately preserved calcareous nannofossil
173 assemblages were found through the lower (~0 m to ~36 m) and uppermost (~68 to ~82 m) parts of the section but are
174 absent through the radiolaritic interval (~36 m to ~52 m) and very poorly preserved in the black shales above the
175 radiolarites (~52 to ~65 m). The first record (FR) of *Hayesites irregularis*, the FR of *Eprolithus floralis* and the last record
176 (LR) of *Conusphaera rothii* (Fig. 2) allowed the identification of the NC5 (part), NC6A, NC6B and NC7 (part) zones of Bralower
177 et al. (1995). The LR of *C. rothii* and the FR of *E. floralis* probably do not correspond with their respective true last and first
178 occurrences, due to the presence of intervals with absence of a calcareous nannofossil record or poorly preserved
179 assemblages linked to low carbonate content (Fig. 2). The onset of the ‘nannoconid crisis’ event was also recorded at ~20
180 m. Two small hiatuses were identified by means of biostratigraphy (see de Gea et al., 2008b for details): the first is linked
181 to the unconformity at the base of the Carbonero formation and the second is located at ~20 m, coinciding with the onset
182 of the ‘nannoconid crisis’ (Fig. 2). The main radiolaritic interval (~36 m to ~52 m) remains unzoned.

183

184 3. Methods

185 3.1. Fieldwork and sampling

186 The Solana de Morales section was re-measured and sampled, with a total of 140 samples taken for bulk geochemical
187 analyses, at an average of 0.6 metres intervals from a total measured thickness of 80 m. Of these, 34 samples at an average
188 of 2.5 meters interval were selected for biomarker analysis, and 47 samples for elemental geochemistry and TOC analyses.
189 Samples for biomarker analyses were packed in aluminium foil in order to avoid contamination from plastics.

190

191 *3.2. C and O isotopes*

192 Bulk C- and O-isotope analyses of the carbonate fraction ($^{13}\text{C}_{\text{carb}}$) of all the collected samples were carried out at the Stable
193 Isotope Laboratory of the University of Michigan, using a Finnigan MAT Kiel IV preparation device coupled directly to the
194 inlet of a Finnigan MAT 253 triple-collector isotope ratio mass spectrometer. The international carbonate standard NBS-
195 19 was used to calibrate to Vienna PeeDee Belemnite (VPDB), with an average precision of 0.15‰. The C-isotope analyses
196 of the total organic fraction ($^{13}\text{C}_{\text{org}}$) of all the collected samples were performed at the Stable Isotope Laboratory (SIDI) of
197 the Universidad Autónoma de Madrid. Samples were treated with 3% HCl for 24 h to remove carbonates and then analysed
198 with a Carlo Erba 1108 elemental analyser coupled to an IRMS VG Isochrom in continuous flow mode. The results were
199 calibrated to the VPDB standard, with a precision better than 0.1‰.

200

201 *3.3. Elemental geochemistry and TOC*

202 34 samples were selected for determination of total organic carbon (TOC) contents. The analyses were performed in the
203 Microanalytical Laboratory at the University of Bristol using a Coulomat 702 Analyser for coulometric determination of
204 Total Carbon and Inorganic Carbon and Eurovector EA3000 Elemental Analyser for nitrogen analyses. The TOC
205 concentration was determined by subtracting the inorganic carbon (IC) concentration from the total carbon (TC) in each
206 sample. A selection of 47 samples was analysed for major and trace elements. Powdered samples were dried at 40°C during
207 24 h and later, 100 mg of sample was acid digested in closed PTFE vessels with a combination of $\text{HNO}_3 + \text{HF} + \text{HClO}_4$ (2.5 ml:
208 5 ml: 2.5 ml v/v). The samples were evaporated and, 1 ml of HNO_3 was added to make a double evaporation. Finally, the
209 sample was re-dissolved and diluted with MilliQ water ($18.2 \text{ M}\Omega\text{cm}^{-1}$) and 1 ml of HNO_3 in a 100 ml volume flask. Analysis
210 were performed using a high resolution inductively coupled plasma-mass spectrometry (HR-ICP-MS, Thermo Scientific,
211 model Element XR). In order to improve the sensitivity of the ICP-MS, a tuning solution containing $1 \mu\text{g}\cdot\text{l}^{-1}$ Li, B, Na, K, Sc,
212 Fe, Co, Cu, Ga, Y, Rh, In, Ba, Tl, U was used, and as internal standard, $20 \text{ mg}\cdot\text{l}^{-1}$ of a monoelemental solution of ^{115}In . The
213 detection limit (DL) was calculated as three times the standard deviation of the average of 10 blanks. The precision of the
214 results was expressed in terms of 2 standard deviation of a set of 8 reference materials measurements. The value of
215 accuracy (%) was calculated using the absolute value of the difference between the measured values obtained during the
216 analysis and the certified values of a set of 8 reference materials analysis. Several commercial solutions were used in order
217 to perform the different calibration curves. These analyses were performed in the Geotop Laboratory of the Institute of

218 Earth Sciences Jaume Almera (Barcelona). Elemental concentrations are expressed as normalized values with respect to Al
219 in order to compensate for the dilution effect (Calvert and Pedersen, 2007).

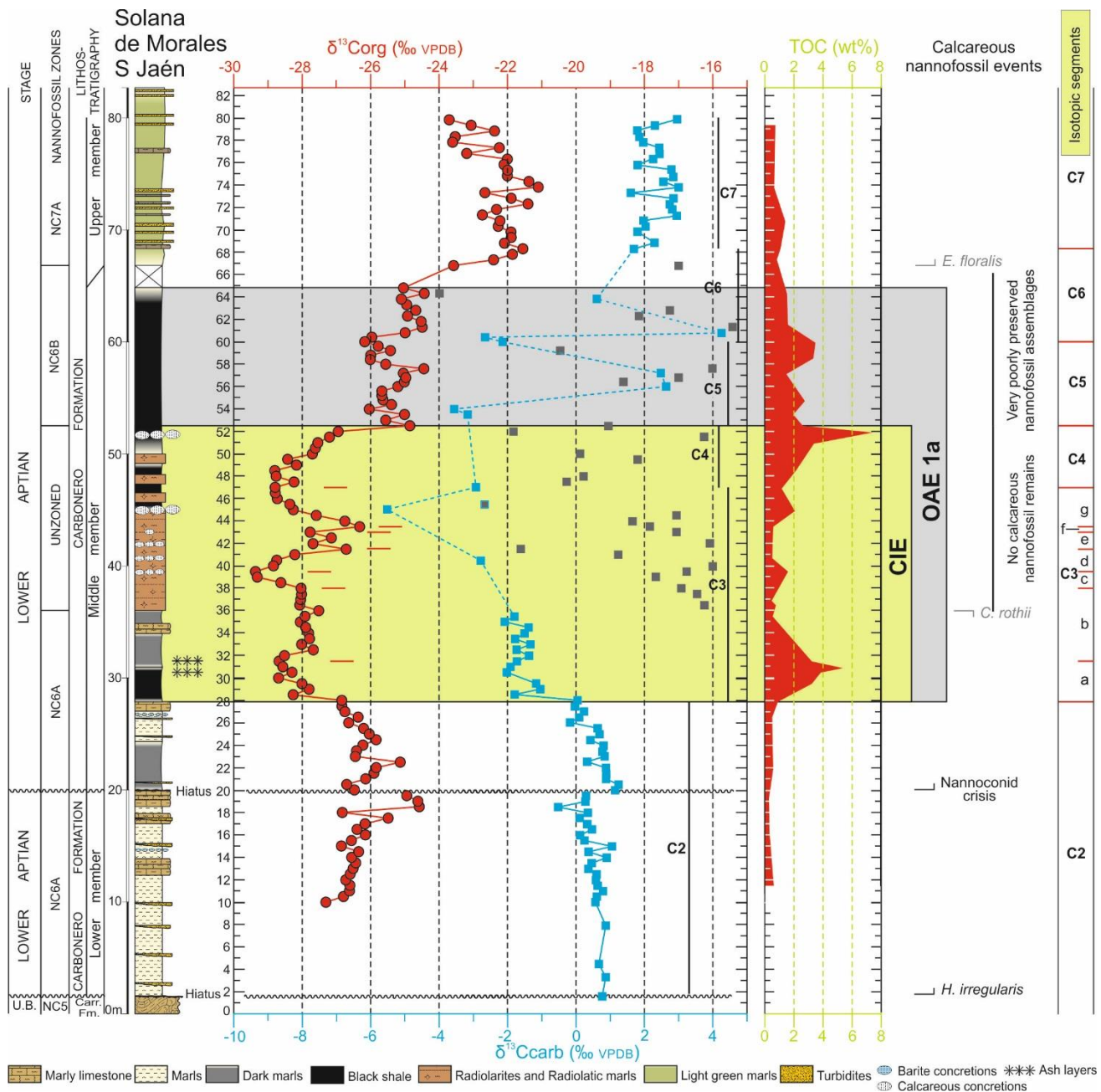
220

221 3.4. Organic geochemistry

222 Initial processing of samples was carried out in the University of Jaén. Bulk rock samples were cleaned with
223 dichloromethane:methanol (DCM:MeOH) 2:1 to remove any contamination from handling. Then samples were coarsely
224 crushed into small pieces (approximately 1 cm) using a mortar and subsequently finely crushed using a ball mill (pre-rinsed
225 with dichloromethane and acetone) at under 400 rpm for 12 minutes. The organic geochemical analyses were performed
226 at the Organic Geochemistry Unit, University of Bristol. The finely ground samples (~30 g) were extracted for 24 h into 200
227 mL of dichloromethane:methanol azeotrope (8:2, v/v; containing activated copper turnings to remove elemental sulphur)
228 using a Soxhlet apparatus. After extraction, the turnings were removed and the samples were concentrated using rotary-
229 evaporation under reduced pressure and dried through a column of sodium sulphate. Total lipid extracts were then
230 separated by flash column chromatography using silica gel and sequential elution with hexane, hexane:dichloromethane
231 (9:1, v/v) and methanol, yielding three fractions containing saturated hydrocarbons, aromatic hydrocarbons, and polar
232 compounds, respectively. The saturated hydrocarbon (containing *n*-alkanes, steranes, and hopanes) and aromatic fractions
233 were analysed by gas chromatography–mass spectrometry (GC–MS) on a Thermo DSQ II gas chromatograph connected to
234 a Thermo Trace Ultra GC–MS. The analytical procedures followed the method described by Quijano et al. (2012).
235 Biomarkers were identified by comparison with published mass spectra and retention times.

236

237 4. Results



238

239 FIGURE. 2. Lithologic column, lithostratigraphical units and calcareous nanofossil biostratigraphy for the Carbonero
 240 section. Calcareous nanofossil zones are after Roth (1978) and Bralower et al. (1995). Stable C-isotope geochemistry
 241 ($\delta^{13}\text{C}_{\text{org}}$ and $\delta^{13}\text{C}_{\text{carb}}$ curves), total organic carbon (TOC) and main biostratigraphic events are also presented. Grey dots
 242 represent not reliable $\delta^{13}\text{C}_{\text{carb}}$ values due to very low carbonate content. The Menegatti et al. (1998) segments (C2–C7) are
 243 indicated in the C-isotope curves. Red arrows within the C3 segment of the $\delta^{13}\text{C}_{\text{org}}$ curve indicate minor shifts used to
 244 differentiate a–g subsegments shown on the right side. The shaded bands correspond to the negative C-isotope excursion
 245 (CIE) and OAE 1a interval. Abbreviations for calcareous nanofossil taxa: *H. irregularis* = *Hayesites irregularis*; *N. truittii* =
 246 *Nannoconus truittii*; *C. rothii* = *Conusphaera rothii*; *E. floralis* = *Eprolithus floralis*.

247 4.1. C-isotope stratigraphy

248 The $\delta^{13}\text{C}_{\text{org}}$ profile displays a distinctive evolution, with a lower part (10 m to 28 m) with relatively stable values of around
249 -27‰ , followed by a broad negative excursion ($2\text{-}3\text{‰}$) between ~ 28 m and 52 m with several successive negative peaks
250 (minima around -29‰). The profile continues with a 2-step positive excursion, reaching around -25‰ in the first step (52.5
251 to 65 m) and maxima of -22 to -21‰ in the second step (65 to 78 m), and finishes with a slight decreasing trend towards
252 $\sim -24\text{‰}$ at the top (Fig. 2).

253 The low abundance of carbonate during most of OAE 1a ($\sim 36\text{-}68$ m) precludes us from generating a reliable high-
254 resolution $\delta^{13}\text{C}_{\text{carb}}$ record. Throughout the intermediate interval (35.5 m–68 m), the obtained $\delta^{13}\text{C}_{\text{carb}}$ values have an erratic
255 distribution due to extremely low carbonate content of most samples ($< 1\%$) (grey square dots in Fig. 2). The $\delta^{13}\text{C}_{\text{carb}}$
256 profile, excluding this intermediate interval, mimics the main fluctuations observed in the $\delta^{13}\text{C}_{\text{org}}$ profile, ranging from ~ 2
257 to -4‰ , with a negative and subsequently positive CIE.

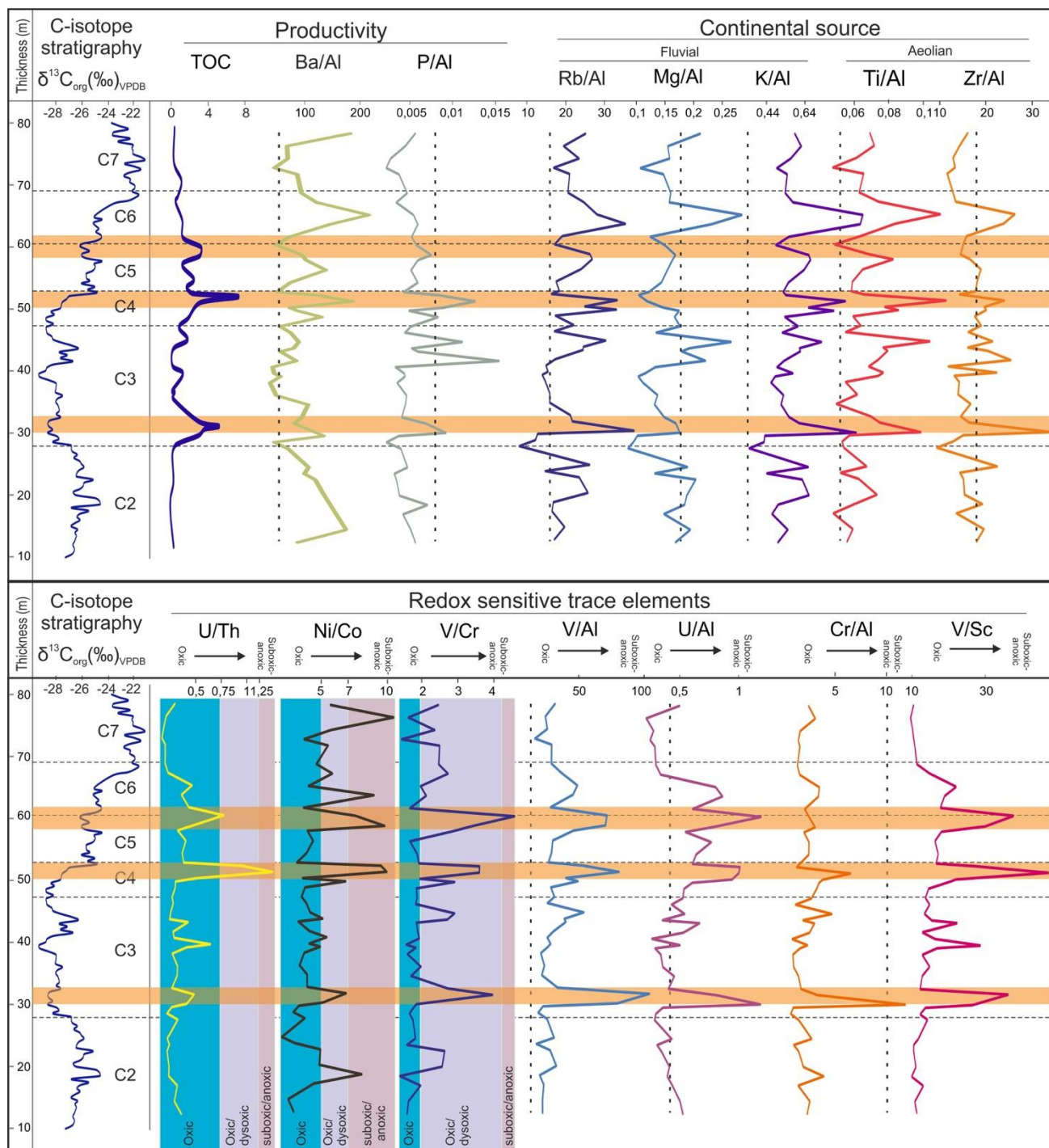
258

259 4.2. Elemental geochemistry

260 Total organic carbon (TOC) fluctuates from 0.2 to 7 wt.%, reaching the highest values at ~ 52 m. Two other intervals with
261 maximum TOC values ($> 2\%$) occur at *i*) ~ 29 m to ~ 35 m, located below the radiolaritic interval, reaching maximum values
262 of 5.1% and *ii*) at 60 m, reaching a maximum of 3.2%. TOC values $< 1\%$ characterize the interval equivalent to the radiolaritic
263 facies (Fig. 2).

264 Abundances of major and trace elements were measured in order to reconstruct changes in the redox conditions,
265 productivity, and terrestrial fluxes. Normalized concentrations are compared to the average shale value (ASV) (Wedepohl,
266 1991; Brumsack, 2006) to estimate level of enrichment or depletion of the analysed elements. Proxies for productivity
267 (TOC, Ba/Al, P/Al), continental sources (Rb/Al, Mg/Al, K/Al, Ti/Al, and Zr/Al), and redox conditions (U/Th, Ni/Co, V/Cr, V/Al,
268 U/Al, Cr/Al and V/Sc) are presented in Fig. 3. Ba/Al and P/Al ratios exhibit more highly variable vertical evolution, with Ba/Al
269 well above the ASV, and P/Al generally below. There is a consistency in the two indices and TOC contents, with all three
270 exhibiting two maxima at 30 m and 51 m. However, a third maximum in TOC (at 58.6 m) corresponds with minima in Ba/Al
271 and P/Al (Fig. 3). The elements selected as proxies for continental sources record high variability through the section, with
272 values generally above the AVS (Rb/Al, K/Al and Ti/Al), or in average within the AVS (Mg/Al and Zr/Al). Collectively, they
273 show a minimum at 28 m, and three maxima at 30–32 m, 49.5–52 m and 61–67 m. Another less pronounced peak is located
274 at 44.5 m (Fig. 3). Redox sensitive trace elements (RSTE) are presented as Al-normalized abundances, as well as the U/Th,

275 Ni/Co and V/Cr indices proposed by Jones and Manning (1994), and the V/Sc index (Kimura and Wanatabe, 1991). All of
 276 the profiles (Fig. 3) show a marked variability through the section, with generally parallel trends, with the exception of the
 277 lowermost part of the section. Three maxima are depicted in all indices, at 30–32.5 m, 49.5–52.5 m and 57.6–61.3 m
 278 (except Cr/Al at 57.6–61.3 m) (Fig. 3). Another smaller maximum occurs from 39.5 to 43.5 in most indices (except U/Th
 279 and Ni/Co).



280

281 FIGURE 3. Stratigraphic distributions of selected elements and elemental ratios. U/Th, Ni/Co and V/Cr indices are
282 plotted following the different oxygen-content zones according to Jones and Manning (1994). Values for Al-normalized
283 elements correspond to Element/Al for major elements and Element/Al x 10⁻⁴ ppm for trace elements. Dashed lines in Al-
284 normalized profiles represent values of the average shale (Wedepohl, 1991; Brumsack, 2006).

285

286 4.3. Organic geochemistry

287 The saturated hydrocarbon fraction is dominated by *n*-alkanes, acyclic isoprenoids, steranes and hopanes, although some
288 samples also contain high-molecular-weight unresolved complex mixtures (UCM).

289

290 4.2.1. *n*-Alkanes

291 The *n*-alkanes are the dominant compounds in most chromatograms, with the *n*-C₁₃ to *n*-C₃₅ homologues being present in
292 most samples. Short chain low-molecular-weight (LMW) components are dominant, with the *n*-C₁₇ to *n*-C₂₁ compounds
293 being the most abundant. To facilitate interpretation of these *n*-alkane distributions, we calculated two different ratios:
294 the HMW/LMW ratio ($[(n\text{-}C_{25} + n\text{-}C_{26} + n\text{-}C_{27} + n\text{-}C_{28} + n\text{-}C_{29}) / (n\text{-}C_{17} + n\text{-}C_{18} + n\text{-}C_{19} + n\text{-}C_{20} + n\text{-}C_{21})]$) in order to
295 constrain the relationship between long and short-chain compounds (Fig. 4); and the carbon preference index (CPI), to
296 obtain an estimate of the thermal maturity (Bray and Evans, 1961). The average HMW/LMW ratio is 0.4 ± 0.1 (Fig. 4), but
297 high variability occurs through the section. It generally decreases from 22 m (0.77) to 52 m (0.24), followed by an increasing
298 trend towards the top (0.52). Imposed on these trends are maxima at 22 m (0.77), 40.8 m (0.54), 53.5 m (0.63) and 73.8
299 m (0.55) (Fig. 4). The CPI ratio has average values of 1.2, with lower values (1.15) during C3 to C5 C-isotope segments, and
300 higher values within the C2 (1.32) and C6-C7 (1.36) segments. These are consistent with thermally mature organic matter.

301

302 4.2.2. Isoprenoids

303 Pristane and phytane, likely derived from the degradation of the phytyl side-chain of chlorophyll, are abundant in all
304 samples and their abundances exhibit high variability through the section. Pr/Ph ratios range from 1.7 to 5.5, with average
305 values of 2.9 ± 0.8 . Values have maxima at 19.25 m and 68.3 m, whereas within the middle interval (37–67 m) values are
306 lower (Fig. 4). The isoprenoids/*n*-alkane ratios were plotted following the classic diagram of Didyck et al (1978) (Fig. 4) in
307 order to infer redox conditions, noting the many caveats associated with this approach (discussed below). Pr/*n*-C₁₇ ratios
308 range between 0.7–2.0, whereas Ph/*n*-C₁₈ ratios are higher but with a similar range of values, between 2–3.2 (Fig. 5).

309

310 4.2.3. Hopanes

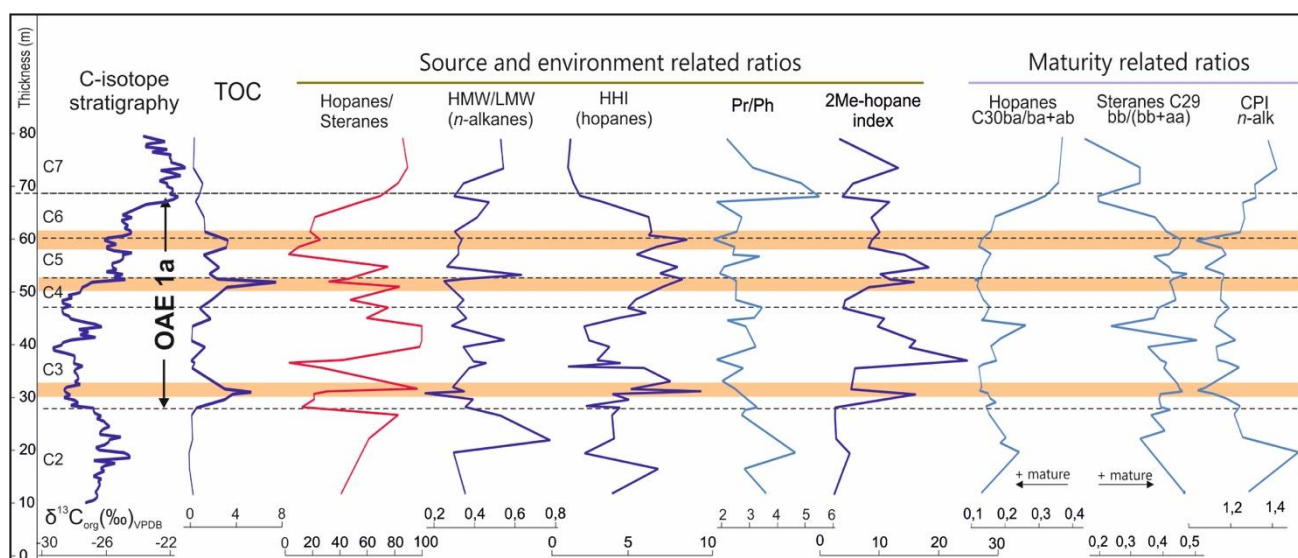
311 Hopanes, the diagenetic and catagenetic products of biohopanoids from diverse bacteria, are present in all samples. There
 312 is a marked increase in relative abundance in the uppermost part of the section. They have a typical, thermally mature
 313 distribution, ranging in carbon number from C₂₇ to C₃₅, with the C₃₀ hopane being the dominant homologue. 17 α ,21 β (H)
 314 hopanes are dominant over the 17 β ,21 α (H) hopanes, and hopanoids with the biological 17 β ,21 β (H) configuration are
 315 absent. The C₃₁-C₃₅ hopanes show the commonly observed decrease in abundance with increasing carbon chain. Other
 316 hopanoids present in all samples are the C₃₁ 2-methylhopanes. In order to analyse stratigraphic trends in the hopane
 317 distributions, several ratios were calculated:

318 (1) The 22S/(22S+22R) homohopane ratio. These ratios are stable through the section, with values of 0.58 and a
 319 standard deviation of 0.02, indicative of high thermal maturity.

320 (2) The C₃₀ $\beta\alpha/(\beta\alpha + \alpha\beta)$ hopane ratio, has an average value of 0.2 (mature organic matter) and its depth profile is
 321 characterized by a marked increase from 58 m upwards to ~0.4 (Fig. 4).

322 (3) The C₃₁ 2-Me-hopane index, 100 x C₃₁ 2-MeHop/(C₃₁ 2-MeHop + C₃₁ Hop) (Summons et al., 1999), ranged from
 323 2 to 25%, with three prominent peaks, at 30.5 m, 37 m and 54.8 m (Fig. 4).

324 (4) The redox sensitive Homohopane index (HHI: the ratio of 100 x C₃₅/(C₃₁ + C₃₅) hopanes, Bishop and Farrimond,
 325 1995; Peters et al., 2005), is generally low but varies between 1% and 10%, with three peaks above 8% at 31 m, 52.4 m
 326 and 60 m (Fig. 4).

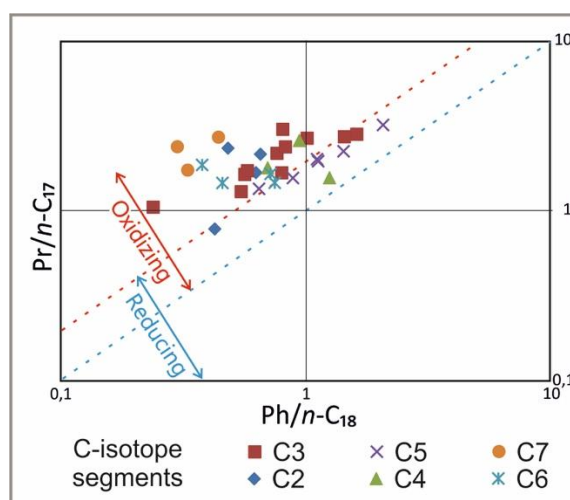


327
 328 FIGURE 4. Biomarker ratios selected as proxies for source and environmental reconstructions and thermal maturity
 329 plotted against C-isotope stratigraphy. See explanation in text.

330

331 4.2.4. Steranes

332 A range of C₂₇ to C₂₉ steranes, derived from alteration of sterols from eukaryotes, are found in all samples. The relative
 333 distributions are similar, with C₂₉ always being dominant (42–58%), but proportions of C₂₉ and C₂₇ increase and those of C₂₈
 334 sterane decrease in the upper part of the section, from 56.8 m upwards. The regular sterane diastereomers are
 335 represented by the four epimers (5 α (H),14 α (H),17 α (H),20R; 5 α (H),14 α (H),17 α (H),20S; 5 α (H),14 β (H),17 β (H),20S and
 336 5 α (H),14 β (H),17 β (H),20R), which are all abundant, with vertical variations in their relative abundance. Furthermore,
 337 13 β ,17 α steranes (diasteranes) are relatively abundant compared to regular steranes. In order to investigate the vertical
 338 variations in the sterane distributions sensitive to thermal maturity we have calculated the C₂₉ $\beta\beta/(\beta\beta+\alpha\alpha)$ ratio, which has
 339 an average value of 0.4 from the base up to 60 m, and then decreases to a minimum of 0.2 around at 70 m with an average
 340 of 0.25 in the interval 60–79 m (Fig. 4). The C₂₉ 20S/(20S+20R) sterane ratio has stable values around 0.5 across the section,
 341 consistent with high thermal maturity. In order to assess the relative proportions of steranes and hopanes, we calculated
 342 the ratio of total hopanes to total steranes (Hopanes/Steranes = C₂₇₋₂₉ steranes/ C₂₇₋₂₉ steranes + C₂₇₋₃₅ hopanes) (Fig. 4).



343
 344 FIGURE 5. Pr/n-C₁₇ vs. Ph/n-C₁₈ plot. Samples from the C2 to C7 C-isotope segments are marked. The reference lines are
 345 from Didyck et al., 1978.

346
 347 **5. Discussion**

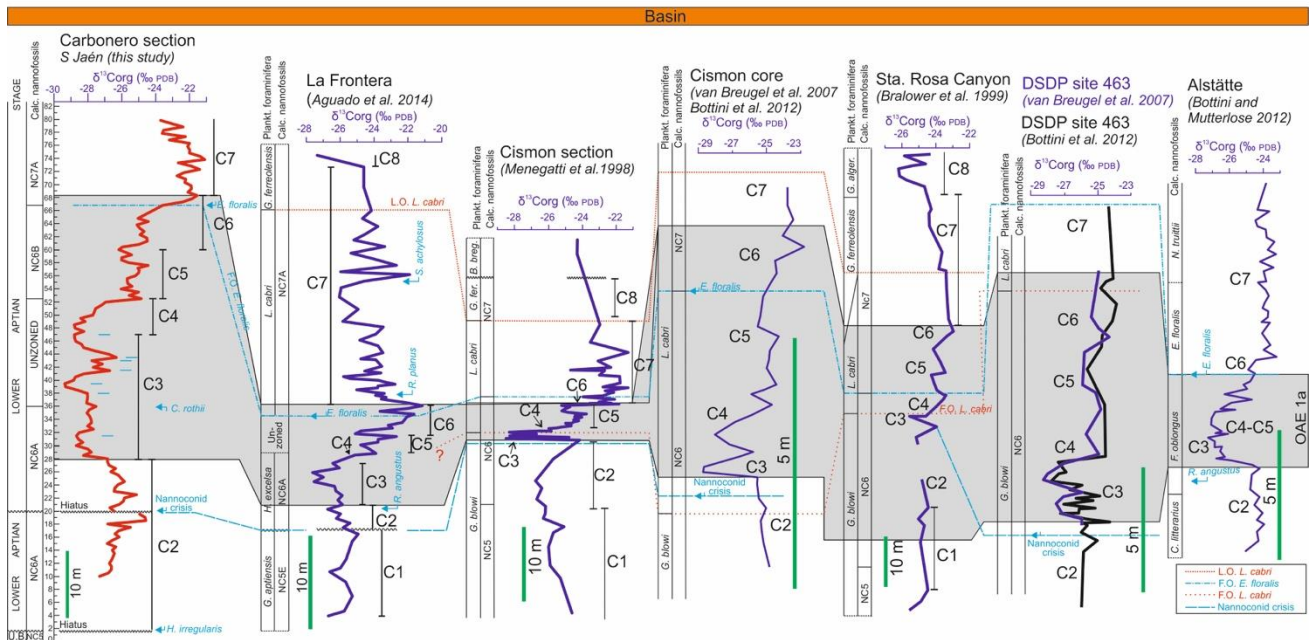
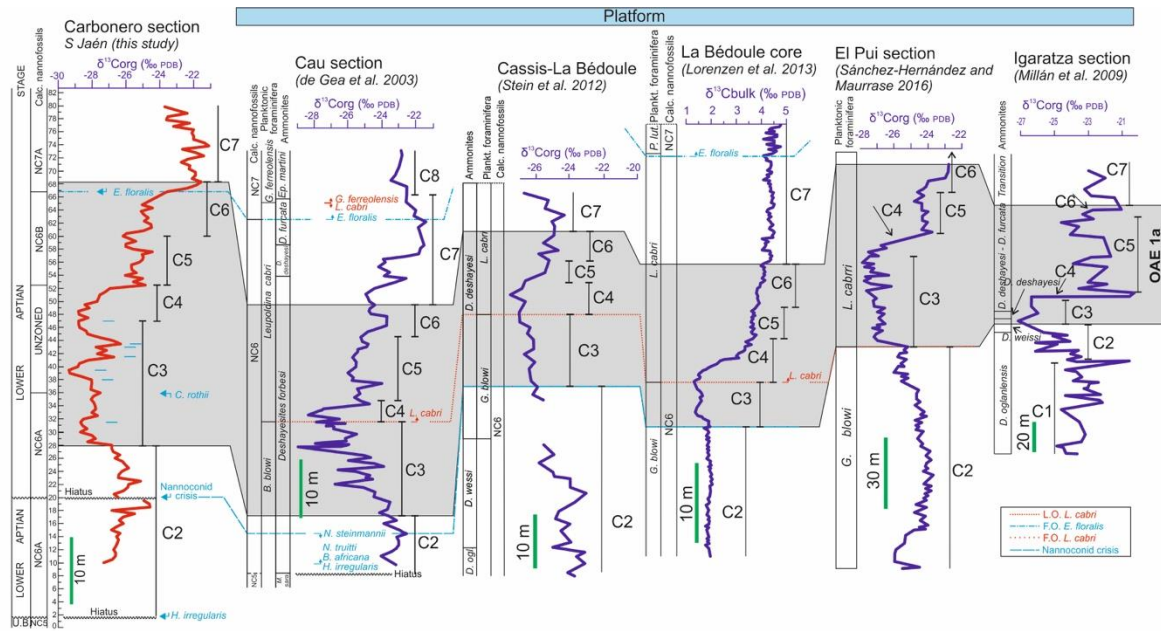
348
 349 *5.1 C-isotope stratigraphy and correlation*

350 Due to the very low proportion of carbonate, the $\delta^{13}\text{C}_{\text{carb}}$ curve has a poor resolution throughout most of the middle
 351 member of the Carbonero Formation (~35-70 m) in the Carbonero section. The $\delta^{13}\text{C}_{\text{org}}$ curve includes expanded and well-
 352 defined trends where the carbon isotope segments C2 (upper part), C3, C4, C5, C6 and C7 (partial) of Menegatti et al.

353 (1998) can be identified (Fig. 2). These segments correlate with other sections (Fig. 6), and allow for the recognition of the
354 early Aptian OAE 1a (~120 Ma) within the middle member of the Carbonero Formation. This is consistent with the
355 sedimentological and biostratigraphic data provided by calcareous nannofossil assemblages (see section 2.2).

356 The interval between 2–28 m, including the complete lower member of the Carbonero Formation plus the
357 lowermost part of its middle member, is assigned to the C2 segment. C-isotope segment C3 in Carbonero is clearly defined
358 by a pronounced negative shift of ~2‰, across 19 metres (28–47 m), similar way to the $\delta^{13}\text{C}$ profile widely identified in the
359 literature (e.g., Menegatti et al., 1998; Erba et al., 1999, 2010; de Gea et al., 2003; Millán et al., 2009; Kuhnt et al., 2011;
360 Bottini and Mutterlose, 2012; Aguado et al., 2014a, b; Bottini et al., 2012, 2015). At Carbonero, the stratigraphic range of
361 segment C3 of 19 m (Fig. 2) is more than 38 times thicker than in the Cismon Core in Southern Alps (Erba et al., 1999),
362 about 7 m thicker than in the Cau section in the Prebetic of SE Spain (de Gea et al., 2003; Moreno-Bedmar et al., 2012;
363 Naafs et al., 2016), and comparable to the thickness of the expanded section of La Bédoule in SE France (Kuhnt et al., 2011;
364 Lorenzen et al., 2013; Moullade et al., 2015). This expanded thickness, joined to a high-density sampling, provides an
365 unprecedented high-resolution record within the C3 segment, where the ‘double trough’ structure, first documented by
366 Van Breugel et al (2007) and evidenced by Lorenzen et al. (2013) is easily identifiable (Fig. 6). As a result, new fluctuations
367 and trends are apparent within the C3 segment of the Carbonero section, showing three distinctive negative peaks at 31.5
368 m, 39.5 m and 47 m, that allow its subdivision into seven subsegments (named ‘a’ to ‘g’ in Fig. 2).

369 A rapid positive excursion in the $\delta^{13}\text{C}$ of ~4‰–5‰ characterizes the C4 segment globally (Menegatti et al., 1998;
370 Kuhnt et al., 2011; Lorenzen et al., 2013; Aguado et al., 2014a, b) (Fig. 2, 7). Similarly, the positive excursion associated
371 with segment C4 in the $\delta^{13}\text{C}_{\text{org}}$ curve at Carbonero has an amplitude of ~4‰ with a thickness of about 5.5 m (47 m–52.5
372 m; Fig. 2). The subsequent stable but, slightly fluctuating and decreasing $\delta^{13}\text{C}_{\text{org}}$ trend (-25 to -26‰) is assigned to segment
373 C5 and has a thickness of ~4.5 m (Fig. 2). A subsequent positive spike $\delta^{13}\text{C}_{\text{org}}$ spike of ~4.5‰ is assigned to segment C6
374 which extends from 60 m to 68.3 m. Finally, the fluctuating and overall decreasing trend from 68.3 m up to the end of the
375 studied section at 80 m (and probably also extending into the overlying succession not covered in this study) is assigned to
376 segment C7.



377

378 FIGURE 6. Correlation of the Carbonero section with selected sections from platform and basinal settings based on $\delta^{13}\text{C}$
 379 stratigraphy. Biostratigraphic key events shown: L.O. *L. cabri* (=last occurrence of *Leupoldina cabri*), F.O. *E. floralis* (= first
 380 occurrence of *Eprolithus floralis*), F.O. *L. cabri* (= first occurrence of *Leupoldina cabri*) and the onset of the nannoconid
 381 crisis.

382

383

384

385

386 The correlation of the $\delta^{13}\text{C}_{\text{org}}$ profile of the Carbonero section with other published records of $\delta^{13}\text{C}_{\text{org}}$ and $\delta^{13}\text{C}_{\text{carb}}$
387 from different basins of pelagic and platform settings are shown in Fig. 6. Sections from pelagic settings are La Frontera,
388 from the Subbetic basin few kilometres away from the Carbonero section (Aguado et al., 2014a, b), Cismon, from the
389 southern Alps, where the C1 to C8 C-isotope segments were defined (Menegatti et al., 1998; Van Breuguel et al., 2007;
390 Bottini et al., 2012), Santa Rosa Canyon in Mexico (Bralower et al., 1999) and Alstätte in NW Germany (Bottini and
391 Mutterlose, 2012). The platform sections are the Cau section in SE Spain (de Gea et al., 2003; Naafs et al., 2016), the Cassis-
392 La Bédoule section (Stein et al., 2012) and La Bédoule core ($\delta^{13}\text{C}_{\text{carb}}$) in southern France (Lorenzen et al., 2013), the El Pui
393 section in the Pyrenees (Sánchez-Hernández and Maurrasse, 2016) and the Igaratza section in the Basque Basin in North-
394 Spain (Millan et al., 2009). The degree of correlation of the various $\delta^{13}\text{C}_{\text{org}}$ profiles is high among the different sections. The
395 main differences are related to the thickness of the C3 segment, which is generally thinner in distal pelagic sections, such
396 as the reference Cismon section and Santa Rosa Canyon, and thicker in platform and continental margin sections such as
397 La Bédoule, Cau, and Carbonero. This variation in thickness is mainly controlled by the subsidence rate but could also reflect
398 high sediment fluxes at marginal sites. Despite the differences in relative thicknesses, the original C-segments, trends, and
399 absolute values of $\delta^{13}\text{C}_{\text{org}}$ are in close agreement between Carbonero, the reference Cismon section and most of the other
400 OAE 1a sections. Importantly, the shape of segment C3 in the Carbonero section, with three negative peaks, is similar to
401 that observed in other expanded sections of the OAE 1a (Cau, Cassis-La Bédoule, El Pui; Fig. 6), and also to the Cismon core
402 where two negative excursions are identified (Van Breuguel et al., 2007; Bottini et al., 2012; Fig.6). Additionally, there are
403 also similar patterns in the TOC profiles with that observed at Cismon, with highest values in C4 after a first maximum at
404 the onset of C3 (Van Breuguel et al., 2007; Bottini et al., 2012). This correlation suggests that the $\delta^{13}\text{C}_{\text{org}}$ profile of the
405 Carbonero section might reflect a global signal and documents fluctuations in the global carbon cycle. The well-defined
406 carbon isotope curve of the Carbonero section provides a robust and highly detailed chemostratigraphic tool for temporal
407 correlation through the lower Aptian, even in the absence of paleontological data in some intervals. It also provides further
408 evidence for complex and episodic input of light carbon release events throughout the C3 interval.

409

410 5.2. Sedimentation rates

411 OAE 1a, defined as the interval C3–C6, has an estimated duration of ~1 to 1.3 Myr (Li et al., 2008; Malinverno et al., 2010;
412 Giraud et al., 2018). The thickness of this interval in Carbonero is 40 m, which gives an average sedimentation rate of 3–4
413 cm/kyr. This sedimentation rate is almost eight times higher than at the Cismon section (0.5 cm/kyr, Li et al., 2008), and it
414 is similar to, although slightly higher, that proposed for the La Bédoule section with values of 2.5–3.2 cm/kyr (Kuhnt et al.,

415 2011; Lorenzen et al., 2013). Although there is a general agreement about the duration of OAE 1a, estimates for the
416 negative excursion (C3 segment) vary from 27–44 kyr (Li et al., 2008) to 22–47 kyr (Malinverno et al., 2010), from the
417 reference Cismon section in the Italian Alps, to >100 kyr from La Bédoule in Southern France (Kuhnt et al., 2011; Lorenzen
418 et al., 2013) and > 300 kyr from sections in central Turkey and the southern Alps (Hu et al., 2012; Huck et al., 2011). These
419 differences are mostly related to the thickness of the C3 segment, which seems to be affected by high condensation in
420 the Cismon section (see Kuhnt et al., 2011; Huck et al., 2011; Hu et al., 2012) potentially related to an acidification event
421 (Erba et al., 2010), but can also be related to other processes. Nevertheless, more recent estimations from the Cismon
422 core suggest a duration of C3 between 100 to 150 kyrs (Bottini et al., 2015). Following the estimates of Malinverno et al
423 (2010) from Cismon for C3 (22–47 kyr), the Carbonero C3 segment (19 m thick) would have a sedimentation rate of ~40–
424 86 cm/kyr, whereas the longer durations from expanded sections would give a sedimentation rate of 5–20 cm/kyr. An
425 extensional tectonic pulse occurred during the early Aptian in the SIP (Martín-Chivelet et al., 2002; Castro et al., 2008;
426 Skelton et al., 2019), which can account for a high subsidence pulse coeval to the deposition of the C3 segment.
427 Nevertheless, following recent estimations from relatively expanded sections (see also Yamamoto et al., 2013), we consider
428 that a duration of >100 kyr, probably in the range of ~300 kyr (as proposed by Huck et al 2011), giving a subsidence rate of
429 ~6 cm/kyr is more consistent with the sedimentary evolution of the Carbonero section (de Gea et al., 2008B). For the
430 segments C4 to C7 there is more agreement about their duration in the literature (Li et al., 2008; Malinverno et al., 2010;
431 Bottini et al., 2015), giving more moderate sedimentation rates in the Carbonero section for the segments C4 (~1.7 cm/kyr),
432 C5 (~1.3 cm/kyr) and C6 (~2.4 cm/kyr), consistent with lower subsidence rates after the main extensional episode on the
433 SIP. Thus, it appears that the C3 interval at Carbonero and other marginal settings was characterised by a dramatic increase
434 in sedimentation rates, as is observed during other rapid warming events such as the PETM (Carmichael et al., 2018, and
435 references therein).

436

437 *5.3. Environmental changes during the early Aptian*

438

439 5.3.1 Elemental geochemistry

440 Distributions and stratigraphic changes in the concentration of selected elements in sediments have been used as marine
441 environmental proxies, specifically for conditions at the sediment/water interface (e.g., Calvert and Pedersen, 2007).
442 Among these environmental conditions, the most commonly investigated are redox state of the ambient seawater,
443 productivity and continental sources, both fluvial and aeolian (e.g., Martínez-Ruiz et al, 2015).

444 Enrichment in RSTE elements is considered to be a pervasive character of sediments deposited under low oxygen
445 conditions and have been used in the investigation of OAEs (Tribovillard et al, 2006; Brumsack, 2006; Calvert and Pedersen,
446 2007; Algeo and Rowe, 2012, Westermann et al., 2010, 2013 among others). Because of the behaviour of RSTE in the water
447 column and during early diagenesis, their sensitivity to redox conditions is rather element-specific, and it is generally
448 recommended that a suite of RSTE (here V, Ni, U, Cr) be used for reconstructing palaeoredox conditions rather than a
449 single element (e.g., Tribovillard et al., 2006; Westermann et al., 2013). In addition to single elements, specific ratios of
450 RSTE have been proposed and used to infer redox conditions (Kimura and Wanatabe, 1991; Jones and Manning, 1994).
451 Chromium, V, Ni, Cr, and U accumulate in marine sediments above their crustal abundances under suboxic conditions, that
452 is in the absence of both oxygen and sulphide (Calvert and Pedersen, 2007). The U/Th, Ni/Co and V/Cr ratios were proposed
453 by Jones and Manning (2004) as indices for the interpretation of bottom water palaeo-oxygen concentrations, which have
454 provided important information on palaeoredox conditions in a large number of studies (e.g., Gallego-Torres et al., 2010;
455 Martinez-Ruiz et al., 2015; Paschal et al., 2019). Jones and Manning (2004) established numerical boundaries between oxic,
456 dysoxic and anoxic conditions, which are represented in Figure 3. The boundary between oxic, suboxic and anoxic
457 conditions as recorded by those ratios varies with different studies (e.g., Hoffman et al., 2008; Algeo and Maynard, 2004),
458 but in general increasing ratios have been correlated with increased anoxia (e.g., Marynowski et al., 2012). V concentration
459 as a redox proxy has been also normalized by Sc (Fig.3), as proposed by Kimura and Wanatabe (1991).

460 The RSTE elements (V, U, Cr) and ratios (U/Th, Ni/Co, V/Cr and V/Sc) at Carbonero show generally parallel
461 distributions across the section (Fig. 5), with three levels of enrichment: at the lower part of the C3 segment, upper part
462 of C4 and C5-C6 transition. In addition to these three distinctive peaks, the evolution of the profiles is rather variable,
463 suggesting instability in redox conditions across the segments C3 to C6 that correspond to the OAE 1a interval. These rapid
464 changes in redox conditions during OAE 1a have been previously detected in other basins of the western Tethys (e.g.,
465 Westermann et al., 2013; Charbonnier et al., 2018), and suggest a general instability with the development of three distinct
466 periods of dysoxia.

467 Marine productivity has been estimated on the basis of geochemical proxies such as total organic carbon (TOC),
468 organic phosphorus (P_{org}), and biogenic barium (Ba_{bio}) (e.g., Tribovillard et al., 2006; Calvert and Pedersen, 2007; Schoepfer
469 et al., 2015). The utility of TOC, P and Ba as palaeomarine productivity proxies depends on a dominantly marine source of
470 organic matter and favourable conditions for preservation in the sediment (Schoepfer et al., 2015). Palaeoproductivity
471 assessments should generally be made on the basis of multiple proxies (e.g., Schoepfer et al., 2015). Organic carbon,
472 representing the single largest constituent of organic matter, provides a direct proxy for productivity (e.g., Pedersen and

473 Calvert, 1990; Schoepfer et al., 2015). Although the concentration of TOC in sediments is also a function of the particle
474 exportation ratio from shallow waters, the preservation of organic matter in the water column and in the sediment, and
475 the dilution of organic carbon by lithogenic or biogenic components in the sediment (e.g., Tyson, 2001; Tribovillard et al.,
476 2006; Calvert and Pedersen, 2007; Schoepfer et al., 2015; Paschal et al., 2019), TOC enrichment is widely used as a primary
477 indicator of marine productivity. Barium has been most widely used as productivity proxy (e.g., Calvert and Pedersen, 2007;
478 Martínez-Ruiz et al., 2015; Schoepfer et al., 2015; Martínez-Ruiz et al., 2019), occurring as barite. The barite has been
479 mainly associated with biogenous aggregates in surface and near-surface waters, especially siliceous debris (Bishop, 1988),
480 although recent studies have demonstrated the link between bacterial activity and marine barite formation through Ba
481 bioaccumulation on microbial biofilms (Martinez-Ruiz et al., 2019). Nevertheless, other minerals can contain Ba, notably
482 lithogenous material derived from crustal rocks; to correct total Ba contents for the contribution from such sources the Ba
483 concentration has been normalized to Al (Calvert and Pedersen, 2007). The behaviour of Ba in sedimentary environments
484 is complex and its interpretation as productivity proxy has several caveats (e.g., Calvert and Pedersen, 2007; Martínez-Ruiz
485 et al., 2015). Schoepfer et al (2015) demonstrated that there is a large negative effect in biogenic barium under conditions
486 of high bulk accumulation rate (BAR), probably due to reduced uptake of barium at the sediment-water interface.
487 Sedimentary barite might undergo diagenetic changes and should be used cautiously as Ba migration is possible under
488 severe sulphate depletion due to microbial sulphate reduction in porewaters (Brumsack et al., 1992), giving rise to the
489 development of barite fronts or nodules (Bréhéret and Brumsack, 2000; Turgeon and Brumsack, 2006). Nevertheless, the
490 variability of sedimentary Ba has become one of the most widely used proxies for palaeoproductivity (Schoepfer et al.,
491 2015). Phosphorus is a limiting macro-nutrient for algal growth, being a structural and functional component of all
492 organisms (Redfield, 1958), and its accumulation in marine sediments has been used as a palaeoproductivity proxy (e.g.,
493 Pedersen and Calvert, 2007). Organic matter is the ultimate source of most P in marine sediments (Schoepfer et al., 2015),
494 whereas detrital P generally comprises less than 20% of total P (Algeo and Ingall, 2007). Consequently, total P is commonly
495 used as a proxy for organically derived phosphorous (Schoepfer et al., 2015). P is preferentially recycled back into the water
496 column under reducing conditions but can be effectively retained within the sediment under oxic to suboxic conditions
497 (Föllmi, 1996; Algeo and Ingall, 2007). As a result of complex interactions between productivity, redox conditions and burial
498 efficiency, P cannot be assumed to have a linear relation with primary productivity (Tribovillard et al., 2006). Nevertheless,
499 P is considered as one of the most robust and widely applicable productivity proxies, being consistently more enriched in
500 productive upwelling zones than in stagnant depositional basins (Brumsack, 2006).

501 The profiles for TOC, Ba/Al and P/Al all three exhibit two peaks in all parameters (lower part of C3 and upper part of C4
502 segments). Ba/Al ratios are generally higher than an average shale (ASV) (Wedepohl, 1991; Brumsack, 2006), which would
503 indicate elevated productivity during OAE 1a, albeit with rapid variations. The presence of barite concretions in the
504 Carbonero section has been related to a diagenetic process of segregation (Molina and Hernández-Molina, 1993) These
505 concretions are present in two levels located within the lower part of the section (C2 segment), but the presence of
506 carbonate concretions within the C3 and C4 segments support the presence of a diagenetic remobilization affecting the
507 section. The positive correlation of Ba and P with TOC in the two lower distinctive peaks shown by most proxies suggest a
508 sedimentary signal in the distribution of Ba, whereas the three intervals of high values recorded only in the Ba/Al ratios
509 which are not correlated by TOC at C2, middle part of C5 and middle part of C6 segments are considered to reflect
510 diagenetic processes of remobilization (Turgeon and Brumsack, 2006). The calcareous nannofossil nutrient index
511 reconstructed for pelagic sections (Aguado et al., 2014a; Bottini et al., 2015; Bottini and Erba, 2018) provide an alternative
512 and independent proxy to evaluate productivity across OAE 1a. Positive peaks of the NI, suggesting high productivity, are
513 recorded at the lower part of C3 segment (Aguado et al., 2014a; Bottini et al., 2015; Bottini and Erba, 2018) and around
514 the C4 isotopic segment (Bottini et al., 2015; Bottini and Erba, 2018), which is in agreement with the indicated by the
515 geochemical productivity proxies in the Carbonero section.

516 The most common element ratios that have been used as proxies for terrigenous supplies are Ti/Al, Zr/Al, K/Al,
517 Mg/Al, Rb/Al, and Si/Al (e.g., Hild and Brumsack, 1998; Niebuhr, 2005; Calvert and Pedersen, 2007; Engelke et al., 2018).
518 The Ti/Al and Zr/Al ratios have been used as a terrestrial aeolian source and grain-size proxy because Ti and Zr concentrate
519 in soils; due to their higher specific gravity than quartz, they are transported with the fine and medium sand quartz in many
520 sediments (Calvert and Pedersen, 2007). We have not used Si/Al ratio because of the presence of radiolarites in the section,
521 which would led to a significant contribution from biogenous Si. K/Al, Rb/Al and Mg/Al have been considered as proxies for
522 fluvial sources (Martínez et al., 2015; Aguado et al., 2016). In the late Quaternary in the Mediterranean, humid periods
523 characterized by lower aeolian input exhibit decreasing Ti/Al and Zr/Al ratios and enhanced K/Al and Mg/Al ratios (e.g.,
524 Warning and Brumsack, 2000; Nijenhuis et al., 2001), suggesting a preferential fluvial source for K and Mg, and an aeolian
525 source for Ti/Al, and Zr/Al (Martínez et al., 2015). However, distinguishing between aeolian and fluvial sources of certain
526 element ratios is difficult because both sources can provide the same detrital minerals (Martínez-Ruiz et al., 2015).

527 To explore the continental inputs, three elements considered as proxies for fluvial sources (Rb/Al, Mg/Al, and K/Al)
528 and two as proxies for aeolian sources (Ti/Al and Zr/Al) have been analysed (Fig. 3). In general, these proxies show parallel
529 patterns, with high-frequency oscillations, and three main peaks at the base of C3, upper part of C4 and middle part of C6

530 segments (Fig. 3). No significant differences are detected between fluvial and aeolian proxies, therefore they are
531 considered collectively as terrestrial proxies. The comparison between profiles of RSTE and productivity proxies reveals
532 interesting relationships: the two lower levels of enrichment in RSTE and productivity proxies are coincident with the
533 enrichment in continental inputs and an inferred increase in sedimentation rates, suggesting a relationship between
534 continental nutrient inputs, productivity and anoxia.

535 Collectively, these data suggest a variable depositional environment during OAE 1a with changes in redox
536 conditions, productivity and continental input. We find three main episodes of enrichment of selected elements. The two
537 first episodes (lower part of C3 and upper part of C4 segment) are related to an increase in productivity, anoxia and
538 continental inputs, suggesting that increased nutrient input from the continent led to an increase in marine productivity,
539 which changed the sedimentary redox conditions. These increases in productivity are also suggested from the calcareous
540 nanofossil-derived NI in pelagic sections (Bottini et al., 2015; Bottini and Erba, 2018). For the first of these events,
541 associated with the lower part of C3, this appears to have been driven by the release of isotopically depleted carbon into
542 the ocean-atmosphere reservoir. The third episode of anoxia/dysoxia (C5/C6 transition), has no evidences of fertilization,
543 as all terrestrial proxies present low values, as well as Ba/Al and P/Al, with the exception of TOC. This decrease in
544 fertilization from the C4 to C5 segments onwards has been also recorded in other sections worldwide (Aguado et al., 2014a;
545 Bottini et al., 2015). In this interval, the data suggest that oxygen depletion led to enhanced preservation of organic matter
546 without a significant increase in productivity, probably related to a restricted water circulation (e.g., Arthur and Sageman,
547 1994; Westermann et al., 2013). This interpretation is also consistent with low P/Al values, as P can be recycled under low
548 oxygen conditions (Föllmi, 1996; Algeo and Ingall, 2007).

549 Enrichments in RSTE, productivity and terrigenous inorganic proxies have been documented in the record of the
550 OAE 1a from different basins, in the Western Tethys (Turgeon and Brumsack, 2006; Stein et al., 2012; Westermann et al.,
551 2013; Charbonnier et al., 2018), Pyrenees (Sánchez-Hernández and Maurrasse, 2016), North German basin (Hild and
552 Brumsack, 1998), Gulf of Mexico (Nuñez-Useche et al., 2015) and Pacific (Erba et al., 2015). These data clearly indicate the
553 development of global perturbations in the marine environmental conditions during OAE 1a, similar to that documented
554 in this study. These perturbations have been also recorded from other OAEs (e.g., OAE2, Westermann et al., 2014), and
555 the PETM (Dickson et al., 2014), indicating to be a relevant feature of hyperthermals.

556

557 5.3.2 Biomarkers

558 5.3.2.1 Maturity assessment

559 Maturity assessment is key to contextualising and interpreting biomarker records (e.g., Peters et al., 2005). The most
560 powerful tools for assessing low to moderate maturity (with respect to oil generation) are those based on the relative
561 distribution of sterane and hopane isomers, along with *n*-alkane distributions. The 22S/(22S+22R) homohopane ratio of
562 c.a. 0.55, the sterane C₂₉ - 20S/(20S+20R) ratio of ~0.5 and the *n*-alkane CPI ratio of c.a. 1, all fairly constant across the
563 section, collectively indicate a thermal maturity of the section near the peak state of oil generation (Mackenzie et al., 1980;
564 Seifert and Moldowan, 1980; Waples and Machihara, 1991). This is equivalent to a vitrinite reflectance between 0.65 and
565 0.85, according to Peters et al (2005). Other ratios more sensitive at this maturity level are C₂₉ steranes (C₂₉ββ/ββ+αα), and
566 C₃₀ hopanes (βα/βα + αβ), which both show a consistent vertical evolution with a slightly high maturity coinciding with the
567 C3 to mid C6 segments interval, that broadly coincides with the OAE 1a interval (Fig. 3). This slight stratigraphic variation
568 in thermal maturity has been also noted across OAE 1a in the Southern Alps (Cismon section; Van Breugel et al., 2007),
569 where the differences are more marked. These authors related these changes to input of organic matter from weathered
570 material from ancient mature rocks, and similar processes could be occurring here, especially given the very high
571 sedimentation rates inferred for C3 as discussed above.

572

573 5.3.2.2 Sources and environment

574 Short-chain *n*-alkanes, as well as pristane and phytane are typically used as indicators for marine organic matter sources,
575 whereas long-chain *n*-alkanes primarily reflect terrigenous sources (Eglinton and Hamilton, 1967). Thermal maturity affects
576 *n*-alkane distributions, mostly the odd to even distributions, which are c.a. 1 in the studied samples, but also reduces the
577 amount of high molecular weight (long-chain) relative to low molecular weight (short-chain) compounds. Given that OM
578 is thermally mature, low HMW/LMW ratios can be explained by the thermal maturity. Nevertheless, the presence of C₂₅-
579 C₃₅ *n*-alkanes in several samples could reflect a terrigenous contribution, which is expected in this depositional setting. If
580 so, the vertical variations in the HMW/LMW ratio could reflect changes in the relative contribution of terrestrial *versus*
581 marine sources. Lowest values indicating highest marine contribution are recorded in the lower part of C3 and upper part
582 of C4 segment. Highest values occur within the C2 and C7 segments, where they are probably biased by a slight decrease
583 in thermal maturity (Fig. 4). Collectively, these data indicate that extracted organic matter derives from mixed terrigenous
584 and marine sources.

585 Steranes are the saturated hydrocarbon derivatives of sterols found in the cell membrane of eukaryotes, particularly
586 marine phytoplankton, and can therefore provide information regarding algal sources (Volkman et al., 1998; Peters, et al.,
587 2005). On the other hand, hopanes are produced by a range of bacteria (Ourisson et al., 1982). The relative contribution

588 of bacterial with respect to algal biomass is usually assessed using the ratio of total hopanes to total steranes [C_{27-30}
589 steranes/(C_{27-30} steranes + C_{27-35} hopanes)] (Moldowan et al., 1985). The hopane/sterane ratio (Fig. 4) exhibits a general
590 increase across the segments C3 to C5, punctuated with abrupt changes. This suggests a long-term but irregular increase
591 in the contribution from bacterial with respect to algal sources during the early parts of OAE 1a. In addition, terrigenous
592 organic matter can deliver hopanes derived from soil bacteria, also increasing the hopane/sterane ratio (e.g., Moldowan
593 et al., 1985).

594 The homohopane index (HHI: C_{35}/C_{31-35} hopanes) is a proxy for changes in redox conditions at the sediment-water
595 interface (Bishop and Farrimond 1995; Peters et al., 2005). In anoxic environments (HHI > 10%), the extended C_{35} side chain
596 is preserved due to sulfurization reactions, whereas shorter side-chain hopanes tend to be more abundant in oxic
597 environments as a result of side chain cleavage during oxidative reactions (Peters and Moldowan 1991; Sinningh  Damst 
598 et al., 1995). The HHI ranges from 1 to 10% (average $6.4\% \pm 2.5$), with two peaks indicating enhanced dysoxia or anoxia in
599 the lower part of C3 segment, and from the uppermost part of C3 to C6, with maxima at the end of C4 and at the C4/C5
600 transition (Fig. 4). Other compounds indicative of anoxia in the water column (e.g., gammacerane and isorenieratane),
601 were not identified, suggesting that the extent of anoxia/dysoxia in the Carbonero basin was relatively limited.

602 The 2 α -methylhopane index (2-MHI) has been used as an indicator of cyanobacterial inputs (Summons et al., 1999),
603 although additional sources have subsequently been reported (Rashby et al., 2007; Welander et al., 2010). Different
604 investigations have pointed out the high concentration of 2-methylhopanoids in sediments deposited during OAEs (Kuypers
605 et al., 2004b; Van Breugel et al., 2007; Blumemberg et al., 2013), as well as during other episodes of environmental change
606 (e.g., Paleocene-Eocene Thermal Maximum, Arregu n et al., 2014). Here, the 2-MHI index shows three main intervals of
607 enrichment, two within the C3 and another at the end of C4 to C5 segments, and other two less pronounced episodes in
608 C6 and C7 segments (Fig 3). Recent research suggests that presence of these compounds might indicate
609 paleoenvironmental stressing conditions, such as hypoxia, changes in pH or nitrogen fixation (Newman et al., 2016; Ricci
610 et al., 2016; Garby et al., 2017). Regardless, our results, alongside similar observations at Shatsky Rise (Dumitrescu and
611 Brassel, 2005) and Cismon (Van Breugel et al., 2007), suggest a similar ecological response to OAE 1a environmental change
612 as that observed for OAE 2, providing additional evidence for mechanistic similarities between these events. However, the
613 Carbonero record, with multiple peaks in 2-MHI suggest a complex series of environmental-ecological interactions.
614 Although these compounds cannot be used as taxonomic biomarkers for any particular group, they may be diagnostic for
615 the confluence of particular environmental parameters such as suboxia or anoxia, high osmolarity and limited fixed
616 nitrogen, collectively indicating ecological stress (Ricci et al., 2016).

617

618 5.3.3 Implications for palaeoenvironmental changes during OAE 1a

619 In order to assess the environmental changes recorded in the studied section and their relation to the perturbations in the
620 global carbon cycle, the evolution of the C-isotope record is compared to the organic and inorganic geochemical records
621 from Carbonero and with published data from different basins worldwide.

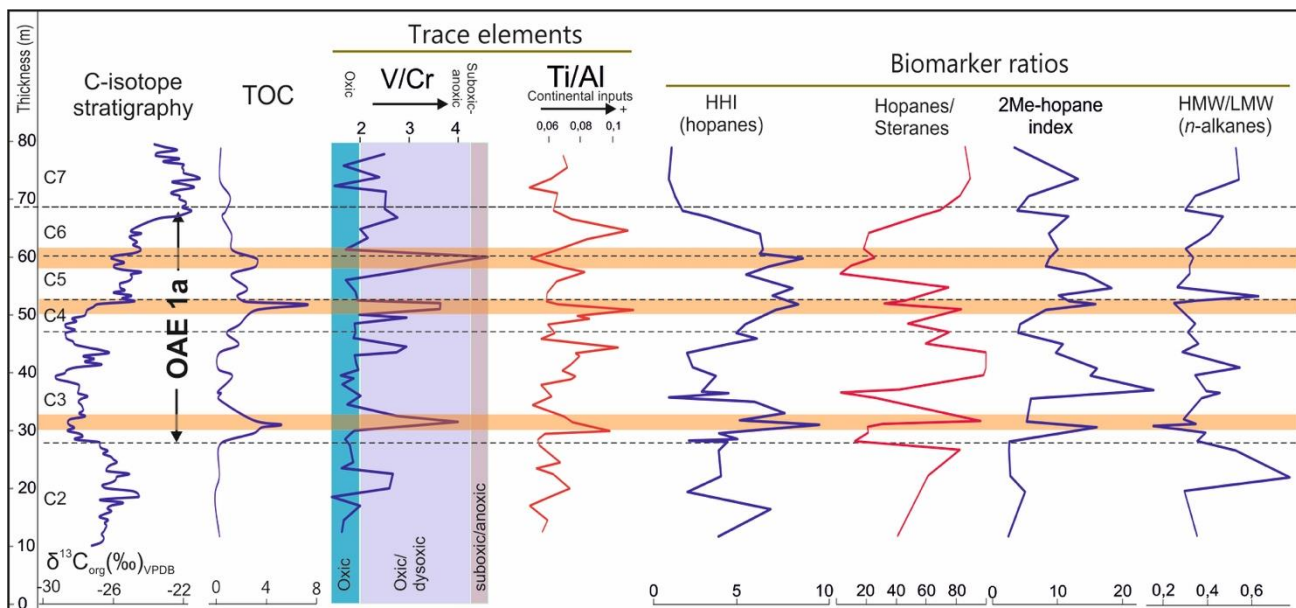
622 The earliest Aptian (C2 isotope segment) exhibits stable values in all parameters analysed, including low
623 concentrations of TOC and RSTE elements, corresponding to low productivity and generally arid environments (Aguado et
624 al 2014a) in a global context of a relatively stable carbon cycle. A regional small discontinuity is recorded in this interval,
625 and the resumption of sedimentation coincides with the onset of the “nannoconid crisis” and a subtle increase in TOC.
626 Calcareous nannofossil assemblages from a nearby section (La Frontera section, Aguado et al., 2014a), record a change to
627 broadly meso-eutrophic surface water conditions and warm climate with intermittent freshening, which was interpreted
628 as a shift towards more humid conditions around this time. This shift can account for a punctual increase in terrestrial
629 inputs recorded in trace elements and biomarkers (HMW/LMW), without a corresponding increase in the productivity
630 proxies. Similar patterns, with a short phase of increased fertility during the C2 segment have been observed in other
631 sections from the tethyan and pacific domains (Bottini et al., 2015)

632 The main change recorded in the Carbonero section corresponds to the negative excursion in $\delta^{13}\text{C}_{\text{org}}$ defining the
633 C3 segment (28-47 m) which shows a complex structure and three negative CIEs. The C3 segment is considered one of the
634 most striking features of OAE 1a and interpreted as the result of an input of light carbon into the ocean/atmosphere system
635 (e.g., Jenkyns, 2010). This carbon is generally thought to come from volcanisms and/or methane hydrate dissociation. One
636 potential way to distinguish between these two mechanisms is the timing, as methane hydrate with lower $\delta^{13}\text{C}$ values can
637 cause a rapid negative excursion through a short-lived release, whereas volcanic CO_2 emissions, with higher $\delta^{13}\text{C}$ values
638 could result in C-isotope negative excursions during gradual and long-lasting episodes (e.g., Mehay et al., 2009; Lorenzen
639 et al., 2013; Naafs et al., 2016). Based on sedimentation rate estimates from expanded sections, including the Carbonero
640 section, the complete negative excursion could have taken more than 100 kyrs. Such a long time span is predominantly
641 consistent with a volcanic CO_2 releasing episode (Naafs et al., 2016), although three abrupt negative CIEs within the C3
642 segment depicted in Carbonero (and other sections) could be related to short pulses of methane release superimposed on
643 a gradual (Jahren et al., 2005; Renard et al., 2005; Mehay et al., 2009; Naafs et al., 2016) or polyphasic (Bottini et al., 2012)
644 volcanic release. The timing of these negative CIEs could be astronomical as has been demonstrated for OAE 2 (Kuypers et

645 al., 2004a; Dickson et al., 2017), although a further analysis of cyclicity in the studied section is needed in order to confirm
646 this hypothesis.

647 The lower part of segment C3 records the first episode of environmental perturbation in the Carbonero section,
648 with RSTE enrichments and increased sedimentation rates coeval with a general perturbation in the biomarker
649 distributions, indicating the development of anoxia/dysoxia near the sediment-water interface, along with an increase in
650 productivity and continental inputs (e.g., Ti/Al) (Fig. 7). Collectively, all of the data point to an increase in fertilization and
651 productivity leading to anoxia/dysoxia and a marked increase of bacterial over algal sources in the organic matter
652 (hopane/sterane index). This is consistent with an intensification of the greenhouse conditions, which may have
653 accelerated the hydrological cycle resulting in increased continental weathering and enhanced nutrient input from the
654 continents to the ocean (Weissert, 1990; Föllmi, 2012; Westermann et al., 2013), which is commonly invoked as a critical
655 aspect of OAE initiation (e.g., Bralower et al., 1999; Erba and Tremolada, 2004; Jenkyns, 2010; Monteiro et al., 2012;
656 Westermann et al., 2013; Aguado et al., 2014a; Bottini et al., 2015). Additional mechanisms have been suggested to
657 contribute to a further fertilization of the ocean, as the relative high sea-level during the early Aptian, which may have
658 favored the reworking of sediments and soils by flooding of land areas (Jarvis et al., 2002; Westermann et al., 2013). The
659 upper part of the C3 segment shows minor punctual increases in terrestrial markers and productivity, under generally well
660 oxygenated waters. In general, the C3 interval is considered to be characterised by increasing $p\text{CO}_2$ concentrations (e.g.,
661 Heimhofer et al 2004; Erba and Tremolada 2004; Erba et al., 2010, 2015; Naafs et al 2016) and temperatures (e.g., Kuhnt
662 et al 2011; Bottini et al., 2015; Naafs and Pancost, 2016). Nevertheless, a short episode of cooling has been proposed
663 during the lower part of C3 segment (Jenkyns 2018), that could be related to a CO_2 drawdown from OM deposition (Bottini
664 et al., 2015; Bottini and Erba, 2018), or to a reduction in the CO_2 volcanic emissions (Bottini et al., 2015).

665 Collectively, the C3 segment records an episode of severe environmental change, with a general gradual increase
666 in $p\text{CO}_2$ probably punctuated by pulses of accelerated rises leading to the spiky shape of the $\delta^{13}\text{C}$ profile recording a marked
667 instability. These changes in $p\text{CO}_2$ and temperatures would have resulted in an intensification of the hydrological cycle, and
668 subsequent increased input of nutrient into the ocean (e.g., Erba, 2004; Föllmi, 2012; Mutterlose and Bottini, 2013;
669 Weissert and Erba 2004; Erba et al., 2015). The high productivity, indicated by the geochemistry but also by the presence
670 of radiolarites within C3 segment, was probably the main factor controlling the oxygen depletion in the bottom waters. In
671 this context, rapid changes in the environmental conditions affected the biomass, giving rise to a dominance of bacteria
672 over algae (Kuypers et al., 2004b).



673
 674 FIGURE 7. Selected elemental and biomarker ratios against C-isotope stratigraphy.

675

676 During the positive C-isotope excursion (segment C4), RSTEs and biomarkers exhibit an increase in anoxic conditions
 677 in the sediment-water interface, coincident with enhanced productivity, and increased terrestrial input, (as indicated by
 678 most of the elemental proxies). Estimated palaeotemperatures suggest a short episode of cooling (Dumitrescu et al., 2006;
 679 Kuhnt et al., 2011; Jenkyns, 2018), due to the decrease in CO₂ concentrations (Heimhofer et al., 2004; Naafs et al., 2016)
 680 associated with either enhanced burial of organic matter or a reduction in the inputs of CO₂ coupled with an increase in
 681 silicate weathering linked to an enhanced hydrological cycle (e.g., Lechler et al., 2015; Jenkyns, 2018). A possible
 682 oxygenation episode during this interval of cooling (Jenkyns, 2018) could correspond to that of the end of C4 segment
 683 recorded in Carbonero (Fig. 4), although further higher-resolution data for correlation are needed to elucidate the
 684 temporal relationships between these environmental changes.

685 The positive C-isotope trend was followed by an interval of stable values in δ¹³C (C5 segment), characterized by a
 686 general recovery to pre-C3 values in most organic and inorganic indices. The exceptions are the 2Me-hopane and the
 687 hopane/sterane indexes, which are elevated in this interval indicating an ongoing ecological perturbation, perhaps related
 688 to environmental stress (Neuman et al., 2016; Ricci et al., 2016). This interval is followed by a third episode of increase in
 689 anoxia/dysoxia during the C5-C6 transition, indicated by enrichment in RSTE and biomarker HHI ratios, but with an
 690 interesting difference to the previous two episodes: in this episode there is no evidence for enhanced productivity nor
 691 terrestrial input (Fig. 7). These results point to a development of anoxia not linked to enhanced production in surface
 692 waters, but instead to possible deoxygenation of the marine bottom waters in the Subbetic basin. This interval is

693 characterized by a further increase in global temperatures (Dumitrescu et al., 2006; Bottini et al., 2015; Naafs and Pancost,
694 2016; Jenkyns, 2018), related to an increase in $p\text{CO}_2$ concentrations (Naafs et al., 2016), probably linked to a sustained
695 input of volcanic CO_2 (e.g., Tejada et al., 2009; Bottini et al., 2012). This evolution of the anoxia/dysoxia during the OAE 1a,
696 from an initial phase controlled by enhanced productivity followed by increased preservation due to the development of
697 anoxia during the OAE 1a can be explained by a model in which fertilization can account for oxygen depletion at a local
698 (basinal) scale (C3 interval), whereas the global consumption of oxygen due to widespread global organic matter
699 deposition, as indicated by the positive excursion in $\delta^{13}\text{C}$ values (C4–C5) would lead to an oxygen depletion in oceanic
700 bottom waters, when a critical threshold is passed as the production of organic matter exceeds the rate in which it is
701 oxidized (Robinson et al., 2004). This evolution from enhanced productivity to enhanced preservation during OAE 1a has
702 been also observed in different sections from the western Tethys (Westermann et al., 2013).

703 During the upper part of C6 and C7 segments, $\delta^{13}\text{C}_{\text{org}}$ values increase (C6) and reach the highest values before they
704 start to decrease (upper part of segment C7). Terrestrial inputs increase during C6, although redox and productivity indices
705 indicate a gradual return towards conditions of well oxygenated waters from the beginning of the C6 segment upwards.
706 Therefore, the highest $\delta^{13}\text{C}$ values are interpreted as the result of enhanced global light carbon burial, although no dysoxic
707 conditions affected the Subbetic Basin, as has been documented from sections worldwide, where the end of the
708 generalized anoxia coincides with the base of C7 segment (e.g., Bottini et al., 2015).

709 Ultimately, as both volcanic inputs and organic burial started to return to pre-OAE conditions, so do oxygenation
710 levels. Intriguingly, however, ecological changes, especially with respect to unicellular organisms (bacteria and algae),
711 persist. Elevated hopane/sterane ratios document a marked increase in bacterial sources over plants and algae, and a
712 further two peaks in 2-Me-hopanes (Fig. 7) collectively indicate an ongoing dominance of OAE-associated microbial
713 assemblages. Thus, the biomass did not completely recover to pre-OAE conditions during the C7 segment, despite the fact
714 that environmental conditions did. A persistent biotic (especially microbial) perturbation has been observed for other
715 events, e.g., the Permo-Triassic Boundary (Xie et al., 2004) and could indicate that recovery of biota would take a longer
716 period, due to persistence of perturbed ecological conditions favoring the microbial growth in the Subbetic basin, probably
717 in relation to a disruption in nutrients cycling (Newman et al., 2016; Ricci et al., 2016; Garby et al., 2017) or grazing pressure
718 (Xie et al., 2004) linked to the effects of the nannoconid crisis, or a combination of both.

719 The general evolution from an initial phase of enhanced productivity followed by increasing preservation, mirrored
720 by climate changes with cooling episodes punctuating the high temperature conditions has been also recorded in other
721 sections worldwide (e.g. Westermann et al., 2014; Bottini et al., 2015; Jenkyns, 2018), collectively indicating a complex

722 global perturbation of the climate and environmental conditions across the OAE 1a. The development of several episodes
723 of potential drawdown of atmospheric CO₂ or reduction in volcanic input of this greenhouse gas leading to episodes of
724 cooling seems to be coeval in different sections worldwide (Jenkyns, 2018), and broadly correlate to the three episodes of
725 maximum anoxia and productivity recorded in the Carbonero section.

726

727 6. Conclusions

728

729 The Carbonero section from the Lower Aptian of the Subbetic basin provides an expanded and continuous
730 stratigraphic record of OAE 1a. The $\delta^{13}\text{C}_{\text{org}}$ stratigraphy records the global C-isotope signal, with identification of previously
731 defined segments. Local subsidence during deposition of segment C3 is considered to be the main cause of differences
732 between sections. Nonetheless, correlation of the C-isotope profile with other sections revealed clear similarities with
733 expanded sections deposited on highly subsiding areas, mostly during the lower part of the OAE 1a, and general agreement
734 during the upper part. In particular, these reveal a far more complex negative carbon isotope excursion, associated with
735 either episodic CO₂ inputs or a complex interplay between carbon inputs to the atmosphere-hydrosphere systems,
736 productivity and preservation of organic matter.

737 Integration of organic and inorganic geochemistry has revealed generally well oxygenated conditions, punctuated
738 by three episodes of anoxia/dysoxia in the water-sediment interface, under a general context of instability in the
739 environmental conditions during the studied interval. The two first episodes of anoxia/dysoxia correlate with enhanced
740 organic productivity during the main negative C-isotope excursion that represents the onset of the OAE 1a. They are placed
741 at the final part of C-isotope negative excursions, probably occurred in response to CO₂ release, increased temperatures
742 and associated hydrological change and weathering, resulting in fertilization-driven oxygen consumption and depletion.
743 This was followed by the widely observed positive carbon isotope excursion, likely due to the burial of OM outpacing
744 volcanic carbon inputs. Interestingly, the third episode of anoxia-dysoxia, which occurred later during the mayor positive
745 C-isotope excursion, is not associated with fertilization, and perhaps instead reflects a general progressive depletion of
746 oxygen during OAE 1a, linked to stagnation of marine waters.

747 The biomarkers distributions have revealed that, although most environmental proxies show a return to pre-OAE
748 conditions during C7 C-isotope segment, a perturbation in microbial ecology persisted, probably indicating a delayed biotic
749 recovery to the perturbation, linked to environmental stress.

750

751 **Acknowledgements**

752

753 This work is a contribution of the research projects CGL2014-55274-P and CGL2014-52546-P of the Spanish Ministry
754 of Science and Technology, and Research Group RNM-200 (Junta de Andalucía). BDAN and RDP were funded by the
755 European Research Council under the European Union's Seventh Framework Programme (FP/2007-2013) / ERC Grant
756 Agreement number 340923 (T-GRES, awarded to RDP). BDAN also received funding through a Royal Society Tata University
757 Research Fellowship. SF thanks the financial support granted for his postdoctoral by Capes (BEX 9085/11-4). Authors wish
758 to thank two anonymous reviewers who improved the manuscript by their useful suggestions.

759

760 **References**

761

- 762 Aguado, R., 1994. Nannofósiles del Cretácico de la Cordillera Bética. Bioestratigrafía, PhD Thesis, Universidad de Granada,
763 Granada, 413 pp.
- 764 Aguado, R., de Gea, G.A., Castro, J.M., O'Dogherty, L., Quijano, M.L., Naafs, B.D.A., Pancost, R.D., 2014a. Late Barremian–
765 early Aptian dark facies of the Subbetic (Betic Cordillera, southern Spain): Calcareous nannofossil quantitative
766 analyses, chemostratigraphy and palaeoceanographic reconstructions. *Palaeogeography, Palaeoclimatology,*
767 *Palaeoecology* 395, 198–221.
- 768 Aguado, R., de Gea, G.A., O'Dogherty, L., 2014b. Integrated biostratigraphy (calcareous nannofossils, planktonic
769 foraminifera, and radiolaria) of an uppermost Barremian–lower Aptian pelagic succession in the Subbetic Basin
770 (southern Spain). *Cretaceous Research* 51, 153–173.
- 771 Aguado, R., Molina, J.M., O'Dogherty, L., 1993. Bioestratigrafía y litoestratigrafía de la Formación Carbonero (Barremiense-
772 Albiense?) en la transición Subbético Externo–Subbético Medio (Sur de Jaén). *Cuadernos de Geología Ibérica* 17,
773 325–344.
- 774 Aguado, R., O'Dogherty, L., Sandoval, J., 2008. Fertility changes in surface waters during the Aalenian (mid Jurassic) of the
775 Western Tethys as revealed by calcareous nannofossils and carbon-cycle perturbations. *Marine*
776 *Micropaleontology* 68, 268–285.
- 777 Aguado, R., Reolid, M., Molina, E., 2016. Response of calcareous nanoplankton to the Late Cretaceous Oceanic Anoxic
778 Event 2 at Oued Bahloul (central Tunisia). *Palaeogeography, Palaeoclimatology, Palaeoecology* 459, 289–305.

- 779 Algeo, T.J., Ingall, E., 2007. Sedimentary Corg:P ratios, Paleocene ventilation, and Phanerozoic atmospheric pO₂.
780 Palaeogeography, Palaeoclimatology, Palaeoecology 256, 130–155.
- 781 Algeo, T.J., Maynard, J.B., 2004. Trace-element behavior and redox facies in core shales of Upper Pennsylvanian Kansas-
782 type cyclothems. Chemical Geology 206, 289-318.
- 783 Algeo T. J., Rowe H., 2012. Paleocyanographic applications of trace-metal concentration data. Chemical Geology 324–325,
784 6–18.
- 785 Ando, A., Kaiho, K., Kawahata, H., Kakegawa, T., 2008. Timing and magnitude of Early Aptian extreme warming: unraveling
786 primary $\delta^{18}\text{O}$ variation in indurated pelagic carbonates at Deep Sea Drilling Project Site 463, central Pacific Ocean.
787 Palaeogeography, Palaeoclimatology, Palaeoecology 260, 463–476.
- 788 Ando, A., Kakegawa, T., Takashima, R., Saito, T., 2002. New perspective on Aptian carbon isotope stratigraphy: data from
789 $\delta^{13}\text{C}$ records of terrestrial organic matter. Geology 30, 227–230.
- 790 Arreguín-Rodríguez, G.J., Alegret, L., Sepúlveda, J., Newman, S. and Summons, R.E., 2014. Enhanced terrestrial input
791 supporting the *Glomospira* acme across the Paleocene-Eocene boundary in Southern Spain. Micropaleontology
792 60, 43–51.
- 793 Arthur M. A. and Sageman B. B., 1994. Marine black shales: depositional mechanisms and environments of ancient
794 deposits. Ann. Rev. Earth Planet. Sci. 22, 499–551.
- 795 Azéma, J., Foucault, A., Fourcade, E., García Hernández, M., González Donoso, J.M., Linares, A., Linares, D., López Garrido,
796 A.C., Rivas, P., Vera, J.A., 1979. Las microfácies del Jurásico y Cretácico de las Zonas Externas de las Cordilleras
797 Béticas. Universidad de Granada (83 pp.).
- 798 Beerling, D.J., Royer, D.L., 2002. Fossil plants as indicators of the Phanerozoic global carbon cycle. Annual Review of Earth
799 and Planetary Sciences 30, 527–556.
- 800 Bishop, J.K.B., 1988. The barite–opal-organic carbon association in oceanic particulate matter. Nature 332, 341–343.
- 801 Bishop, N., Farrimond, P., 1995. A new method of comparing extended hopane distributions. Organic Geochemistry 23,
802 987–990.
- 803 Blättler, C.L., Jenkyns, H.C., Reynard, L.M., Henderson, G.M., 2011. Significant increases in global weathering during
804 Oceanic Anoxic Events 1a and 2 indicated by calcium isotopes. *Earth and Planetary Science Letters* 309, 77-88.
805 <https://doi.org/10.1016/j.epsl.2011.06.029>

806 Blumenberg, M., Berndmeyer, C., Moros, M., Muschalla, M., Schmale, O., Thiel, V., 2013. Bacteriohopanepolyols record
807 stratification, nitrogen fixation and other biogeochemical perturbations in Holocene sediments of the central
808 Baltic Sea. *Biogeosciences* 10, 2725–2735.

809 Bottini, C., Cohen, A.S., Erba, E., Jenkyns, H.C., Coe, A.L., 2012. Osmium isotope evidence for volcanism, weathering and
810 ocean mixing during the early Aptian OAE 1a. *Geology* 40, 583–586. <https://doi.org/10.1130/G33140.1>

811 Bottini, C., Erba, E., 2018. Mid-Cretaceous paleoenvironmental changes in the western Tethys. *Climate of the Past* 14,
812 1147–1163. <https://doi.org/10.5194/cp-14-1147-2018>

813 Bottini, C., Erba, E., Tiraboschi, D., Jenkyns, H.C., Schouten, S., Sinninghe Damsté, J.S., 2015. Climate variability and ocean
814 fertility during the Aptian Stage. *Climate of the Past* 11 (3), 383–402. <https://doi.org/10.5194/cp-11-383-2015>

815 Bottini, C., Mutterlose, J., 2012. Integrated stratigraphy of Early Aptian black shales in the Boreal Realm: calcareous
816 nanofossil and stable isotope evidence for global and regional processes. *Newsletters on Stratigraphy* 45, 115–
817 137.

818 Bralower, T.J., CoBabe, E., Clement, B., Sliter, W.V., Osburn, C.L., Longoria, J., 1999. The record of global change in Mid-
819 Cretaceous (Barremian–Albian) sections from the Sierra Madre, northeastern Mexico. *Journal of Foraminiferal*
820 *Research* 29, 418–437.

821 Bralower, T.J., Leckie, R.M., Sliter, W.V., Thierstein, H.R., 1995. An integrated Cretaceous microfossil biostratigraphy. *The*
822 *Society of Economic Paleontologists and Mineralogists Special Publication* 54, 65–79.

823 Bray, E.E., Evans, E.D. 1961. Distribution of n-paraffins as a clue to recognition of source beds. *Geochimica et Cosmochimica*
824 *Acta*, 22, 2–15. [https://doi.org/10.1016/0016-7037\(61\)90069-2](https://doi.org/10.1016/0016-7037(61)90069-2)

825 Bréhéret, J.G., Brumsack, H.J., 2000. Barite concretions as evidence of pauses in sedimentation in the Marnes Bleues
826 Formation of the Vocontian Basin (SE France). *Sedimentary Geology* 130, 205–228.

827 Brumsack, H.J., 2006. The trace metal content of recent organic carbon-rich sediments: implications for Cretaceous black
828 shale formation. *Palaeogeography, Palaeoclimatology, Palaeoecology* 232, 344–361.

829 Brumsack, H.J., Zuleger, E., Gohn, E., Murray, R.W., 1992. Stable and radiogenic isotopes in pore waters from Leg 127,
830 Japan Sea. In: Pisciotta, K.A., Ingle Jr., J.C., von Breymann, M.T., Barron, J., et al. (Eds.), *Proc. Ocean Drill. Project*
831 *127/128 Part 1*, pp. 635–650.

832 Calvert, S.E., Pedersen, T.F., 2007. Chapter Fourteen-Elemental Proxies for Palaeoclimatic and Palaeoceanographic
833 Variability in Marine Sediments: Interpretation and Application. In: *Developments in Marine Geology* 1, pp. 567–
834 644.

835 Carmichael, M.J., Pancost, R.D., Lunt, D.J. 2018. Changes in the occurrence of extreme precipitation events at the
836 Paleocene–Eocene thermal maximum. *Earth and Planetary Science Letters*, 501, 24-36. [https://doi.org/](https://doi.org/10.1016/j.epsl.2018.08.005)
837 10.1016/j.epsl.2018.08.005

838 Castro, J.M., de Gea, G.A., Ruiz-Ortiz, P.A., Nieto, L.M., 2008. Development of carbonate platforms on an extensional (rifted)
839 margin. The Valanginian–Albian record of the Prebetic of Alicante (SE Spain). *Cretaceous Research* 29, 848–860.

840 Charbonnier, G., Adatte, T., Spangenberg, J.E., Föllmi, K.B., 2018. The expression of early Aptian to latest Cenomanian
841 oceanic anoxic events in the sedimentary record of the Briançonnais domain. *Global and Planetary Change* 170,
842 76–92.

843 Chumakov, N.M., Zharkov, M.A., Herman, A.B., Doludenko, M.P., Kalandadze, N.N., Lebedev, E.L., Ponomarenko, A.G.,
844 Rautian, A.S., 1995. Climatic belts of the mid-Cretaceous time. *Stratigraphy and Geological Correlation* 3, 241–
845 260.

846 de Gea, G.A., 2004. Bioestratigrafía y eventos del Cretácico Inferior en las Zonas Externas de la Cordillera Bética. PhD thesis,
847 Universidad de Jaén, Servicio de Publicaciones de la Universidad de Jaén, 658 pp.

848 de Gea, G.A., Aguado, R., Castro, J.M., 2008a. Variaciones en el registro isotópico del carbono en dos secciones de edad
849 Aptiense inferior en la zona de transición entre el Subbético Externo y el Subbético Medio (Cordilleras Béticas,
850 Provincia de Jaén). *Geogaceta* 44, 191–194.

851 de Gea, G.A., Aguado, R., Castro, J.M., Molina, J.M., O'Dogherty, L., Ruiz Ortiz, P.A., 2008b. Lower Aptian Subbetic organic-
852 rich facies, radiolarites and associated deposits: the local expression of Oceanic Anoxic Event 1a (Carbonero
853 Formation, southern Spain). *Cretaceous Research* 29, 861–870.

854 de Gea, G.A., Aguado, R., Castro, J.M., Molina, J.M., Ruiz Ortiz, P.A., 2008c. Registro del evento anóxico del Aptiense inferior
855 en la cuenca subbética (Sur de Jaén): La Formación Carbonero. *Geotemas* 10, 135–138.

856 de Gea, G.A., Castro, J.M., Aguado, R., Ruiz Ortiz, P.A., Company, M., 2003. Lower Aptian carbon-isotope stratigraphy from
857 a distal carbonate shelf setting: the Cau section, Prebetic Zone, SE Spain. *Palaeogeography, Palaeoclimatology,*
858 *Palaeoecology* 200, 207–219.

859 Demaison, G.J., Moore, G.T., 1980. Anoxic environments and oil source bed genesis. *Organic Geochemistry* 2, 9–31.

860 Dickson, A. J., Rees-Owen, R., März, L.C., Coe, A.L., Cohen, A.S., Pancost, R.D., Taylor, K., Shcherbinina, E., 2014. The spread
861 of marine anoxia on the northern Tethys margin during the Paleocene-Eocene Thermal Maximum.
862 *Paleoceanography* 29, 471–488. <https://doi.org/10.1002/2014PA002629>.

863 Dickson, A.J., Saker-Clark, M., Jenkyns, H.C., Bottini, C., Erba, E., Russo, F., Gorbanenko, O., Naafs, B.D.A., Pancost, R.D.,
864 Robinson, S.A., van den Boorn, S.H.J.M., Idiz, E., 2017. A Southern Hemisphere record of global trace-metal
865 drawdown and orbital modulation of organic-matter burial across the Cenomanian–Turonian boundary (Ocean
866 Drilling Program Site 1138, Kerguelen Plateau). *Sedimentology*, 64 (1), 186-203.
867 <https://doi.org/10.1111/sed.12303>

868 Didyck, B.M., Simoneit, B.R.T., Brassel, S.C., Eglinton, G., 1978. Organic geochemical indicators of palaeoenvironmental
869 conditions of sedimentation. *Nature* 272, 216–222.

870 Dumitrescu, M., Brassell, S.C., 2005. Biogeochemical assessment of sources of organic matter and paleoproductivity during
871 the Early Aptian Oceanic Anoxic Event at Shatsky Rise, ODP Leg 198. *Organic Geochemistry* 36, 1002–1022.

872 Dumitrescu, M., Brassell, S.C., Schouten, S., Hopmans, E.C., Sinninghe-Damste, J.S., 2006. Instability in tropical Pacific sea-
873 surface temperatures during the early Aptian. *Geology* 34, 833–836.

874 Eglinton, G., Hamilton, R.J., 1967. Leaf epicuticular waxes. *Science* 156, 1322–1335.

875 Engelke, J., Linnert, C., Niebuhr, B., Schnetger, B., Brumsack, H.J., Mutterlose, J., Wilmsen, M., 2018. Tracking Late
876 Cretaceous environmental change: Geochemical environment of the upper Campanian to lower Maastrichtian
877 chalks at Krons Moor, northern Germany. *Cretaceous Research* 84, 323-339. [https://doi.org/](https://doi.org/10.1016/j.cretres.2017.10.00)
878 [0.1016/j.cretres.2017.10.00](https://doi.org/10.1016/j.cretres.2017.10.00)

879 Erba, E., 1994. Nannofossils and superplumes: The early Aptian 'nannoconid crisis'. *Paleoceanography* 9, 483–501.
880 <https://doi.org/10.1029/94PA00258>.

881 Erba, E., Bottini, C., Weissert, H.J., Keller, C.E., 2010. Calcareous nannoplankton response to surface-water acidification
882 around Oceanic Anoxic Event 1a. *Science* 329, 428–432.

883 Erba, E., Channell, J.E.T., Claps, M., Jones, C., Larson, R., Opdyke, B., Premoli Silva, I., Riva, A., Salvini, G., Torricelli, S., 1999.
884 Integrated stratigraphy of the Cismon APTICORE (Southern Alps, Italy): a "reference section" for the Barremian–
885 Aptian interval at low latitudes. *Journal of Foraminiferal Research* 29, 371–391.

886 Erba, E., Duncan, R.A., Bottini, C., Tiraboschi, D., Weissert, H., Jenkyns, H.C., Malinverno, A., 2015. Environmental
887 consequences of Ontong Java Plateau and Kerguelen Plateau volcanism. In: *The Origin, Evolution, and*

888 Environmental Impact of Oceanic Large Igneous Provinces (C.R. Neal, W.W. Sager, T. Sano, T., y E. Erba, eds.).
889 Geological Society of America Special Paper 511.

890 Erba, E., Tremolada, F., 2004. Nannofossil carbonate fluxes during the Early Cretaceous: phytoplankton response to
891 nutrification episodes, atmospheric CO₂, and anoxia. *Paleoceanography* 19. <https://doi.org/10.1029/2003PA00084>
892 (PA1008).

893 Föllmi, K.B., 1996. The phosphorus cycle, phosphogenesis and marine phosphate-rich de- posits. *Earth Science Reviews* 40,
894 55–124.

895 Föllmi, K.B., 2012. Early Cretaceous life, climate and anoxia. *Cretaceous Research* 35, 230–257.

896 Föllmi, K.B., Godet, A., Bodin, S., Linder, P., 2006. Interactions between environmental change and shallow water carbonate
897 buildup along the northern Tethyan margin and their impact on the Early Cretaceous carbon isotope record.
898 *Paleoceanography* 21, PA4211 <https://dx.doi.org/10.1029/2006PA001313>.

899 Foster, G.L., Hull, P., Lunt, D.J., Zachos, J.C., 2018. Placing our current ‘hyperthermal’ in the context of rapid climate change
900 in our geological past. *Royal Society of London Philosophical Transactions. A* 376: 20170086.
901 <https://dx.doi.org/10.1098/rsta.2017.0086>

902 Gallego-Torres, D., Martínez-Ruiz, F., De Lange, G.J., Jimenez-Espejo, F.J., Ortega-Huertas, M., 2010. Trace-elemental
903 derived paleoceanographic and paleoclimatic conditions for Pleistocene Eastern Mediterranean sapropels.
904 *Palaeogeography, Palaeoclimatology, Palaeoecology* 293, 76-89.

905 Garby, T.J., Matys, E.D., Ongley, S.E., Salih, A., Larkum, A.W., Walter, M.R., Summons, R.E., Neilan, B.A., 2017. Lack of
906 methylated hopanoids renders the cyanobacterium *Nostoc punctiforme* sensitive to osmotic and pH stress.
907 *Applied and Environmental Microbiology*, 83 (13), <https://doi.org/10.1128/AEM.00777-17>

908 García-Hernández, M., López Garrido, A.C., Sanz de Galdeano, C., Vera, J.A., Rivas, P., 1980. Mesozoic paleogeographic
909 evolution in the External Zones of the Betic Cordillera (Spain). *Geologie en Mijnbouw* 59, 155–168.

910 Giraud, F., Pittet, B., Grosheny, D., Baudin, F., Lécuyer, C., Sakamoto, T., 2018. The palaeoceanographic crisis of the Early
911 Aptian (OAE 1a) in the Vocontian Basin (SE France). *Palaeogeography, Palaeoclimatology, Palaeoecology* 511, 483-
912 505. <https://doi.org/10.1016/j.palaeo.2018.09.014>

913 Gröcke, D.R., Hesselbo, S.P., Jenkyns, H.C., 1999. Carbon-isotope composition of Lower Cretaceous fossil wood: ocean–
914 atmosphere chemistry and relation to sea-level change. *Geology* 27, 155–158.

915 Hay, W., 2017. Toward understanding Cretaceous climate—An updated review. *Science China Earth Sciences* 60, 5-19.

916 Heimhofer, U., Hochuli, P.A., Herrle, J.O., Andersen, N., Weissert, H., 2004. Absence of major vegetation and
917 palaeoatmospheric pCO₂ changes associated with oceanic anoxic event 1a (Early Aptian, SE France). *Earth and*
918 *Planetary Science Letters* 223, 303–318.

919 Heldt, M., Mutterlose, J., Berner, U., and Erbacher, J., 2012. First high-resolution δ¹³C-records across black shales of the
920 Early Aptian Oceanic Anoxic Event 1a within the mid-latitudes of northwest Europe (Germany, Lower Saxony
921 Basin). *Newsletters on Stratigraphy*, 45, 151–169.

922 Hild, E., Brumsack, H.J., 1998. Major and minor element geochemistry of Lower Aptian sediments from the NW German
923 Basin (core Hoheneggelsen KB 40). *Cretaceous Research* 19, 615-633. DOI: 10.1006/cre.1998.0122

924 Hochuli, P.A., Menegatti, A.P., Weissert, H., Riva, A., Erba, E., Premoli Silva, I., 1999. Episodes of high productivity and
925 cooling in the early Aptian Alpine Tethys. *Geology* 27, 657–660.

926 Hoffman, D., Algeo, T.J., Maynard, B., Joachimski, M.M., Hower, J.C., Jaminski, J., 1998. Regional and stratigraphic variation
927 in bottomwater anoxia in offshore core shales of Upper Pennsylvanian cyclothems from the Eastern Midcontinent
928 Shelf (Kansas), USA. In: Schieber, J., Zimmerle, W., Sethi, P.S. (Eds.), *Shales and Mudstones*. 1. Schweizerbartische
929 Verlagsbuchhandlung, Stuttgart, Germany, pp. 243–269.

930 Hu, X., Zhao, K., Yilmaz, I.O., Li, Y., 2012. Stratigraphic transition and palaeoenvironmental changes from the Aptian oceanic
931 anoxic event 1a (OAE1a) to the oceanic red bed 1 (ORB1) in the Yenicesihlar section, central Turkey. *Cretaceous*
932 *Research* 38, 40–51.

933 Huck, S., Heimhofer, U., Rameil, N., Bodin, S., Immenhauser, A., 2011. Strontium and carbon-isotope chronostratigraphy
934 of Barremian–Aptian shoal-water carbonates: Northern Tethyan platform drowning predates OAE 1a. *Earth and*
935 *Planetary Science Letters* 304, 547–558.

936 Jahren, A.H., Conrad, C.P., Crystal Arens, N., Mora, G., Lithgow-Bertelloni, C., 2005. A plate tectonic mechanism for
937 methane hydrate release along subduction zones. *Earth and Planetary Science Letters* 236, 691–704.

938 Jarvis, I., Lignum, J.S., Gröcke, D.R., Jenkyns, H.C., Pearce, M.A., 2011. Black shale deposition, atmospheric CO₂ drawdown,
939 and cooling during the Cenomanian–Turonian Oceanic Anoxic Event. *Paleoceanography* 26, PA3201.
940 <https://doi.org/10.1029/2010PA002081>

941 Jarvis I., Mabrouk A., Moody R. T. J., de Cabrera S., 2002. Late Cretaceous (Campanian) carbon isotope events, sea-level
942 change and correlation of the Tethyan and Boreal realms. *Palaeogeography, Palaeoclimatology, Palaeoecology*
943 188, 215–248.

944 Jenkyns, H.C., 1995. Carbon isotope stratigraphy and paleoceanographic significance of the Lower Cretaceous shallow
945 water carbonates of Resolution Guyot, mid-Pacific Mountains. In: Winterer, E.L., Sager, W.W., Firth, V.J., Sinton,
946 M. (Eds.), *Proceedings of the Ocean Drilling Program, Scientific Results*, 143. College Station, Texas, pp. 89–97.

947 Jenkyns H. C., 1999. Mesozoic anoxic events and palaeoclimate. *Zentralblatt für Geologie und Paläontologie* 1997, 943–
948 949.

949 Jenkyns, H.C., 2003, Evidence for rapid climate change in the Mesozoic–Palaeogene greenhouse world. *Royal Society of*
950 *London Philosophical Transactions, A*. 361, 1885–1916. <https://doi.org/10.1098/rsta.2003.1240>

951 Jenkyns, H.C., 2010. Geochemistry of oceanic anoxic events. *Geochemistry Geophysics Geosystem* 11, Q03004.
952 <https://doi.org/10.1029/2009GC002788>.

953 Jenkyns, H.C., 2018. Transient cooling episodes during Cretaceous Oceanic Anoxic Events with special reference to OAE 1a
954 (Early Aptian). *Phil. Trans. R. Soc. A* 376: 20170073. <https://dx.doi.org/10.1098/rsta.2017.0073>

955 Jones, B.A., Manning, D.A.C., 1994. Comparison of geochemical indices used for the interpretation of palaeoredox
956 conditions in ancient mudstones. *Chemical Geology* 111, 111–129.

957 Jones., C.E., Jenkyns, H.C., 2001. Seawater strontium isotopes, oceanic anoxic events, and seafloor hydrothermal activity
958 in the Jurassic and Cretaceous. *American Journal of Science* 301, 112–149. <https://doi.org/10.2475/ajs.301.2.112>

959 Kidder, D.L., Worsley, T.R., 2010. Phanerozoic Large Igneous Provinces (LIPs), HEATT (Haline Euxinic Acidic Thermal
960 Transgression) episodes, and mass extinctions. *Palaeogeography, Palaeoclimatology, Palaeoecology* 295, 162–191.
961 <https://doi.org/10.1016/j.palaeo.2010.05.036>

962 Kimura, H., Wanatabe, Y., 1991. Oceanic anoxia at the Precambrian-Cambrian boundary. *Geology* 29, 995–998.

963 Kuhnt, W., Holbourn, A., Moullade, M., 2011. Transient global cooling at the onset of early Aptian oceanic anoxic event
964 (OAE) 1a. *Geology* 39, 323–326.

965 Kump, L.R., Brantley, S.L., Arthur, M.A., 2000. Chemical weathering, atmospheric CO₂, and climate. *Annu. Rev. Earth Planet.*
966 *Sci.* 28, 611–667. <https://doi.org/10.1146/annurev.earth.28.1.611>

967 Kuypers, M.M., Lourens, L., Rijpstra, W.I.C., Pancost, R.D., Nijenhuis, I.A., Sinninghe-Damsté, J.S., 2004a. Orbital forcing of
968 organic carbon burial in the proto-North Atlantic during Oceanic Anoxic Event 2. *Earth and Planetary Science*
969 *Letters* 228, 465–482.

970 Kuypers, M.M., van Breugel, Y., Schouten, S., Erba, E., Sinninghe Damsté, J.S., 2004b. N₂-fixing cyanobacteria supplied
971 nutrient N for Cretaceous oceanic anoxic events. *Geology* 32, 853-856.

972 Larson, R.L., and Erba, E., 1999. Onset of the mid-Cretaceous greenhouse in the Barremian–Aptian: Igneous events and the
973 biological, sedimentary and geochemical responses. *Paleoceanography* 14, 663–678.
974 <https://doi.org/10.1029/1999PA900040>

975 Lechler, M., Pogge von Strandmann, P.A.B, Jenkyns, H.C., Prossera, G. Parente, M., 2015. Lithium-isotope evidence for
976 enhanced silicate weathering during OAE1a (Early Aptian Selli event). *Earth and Planetary Science Letters* 432,
977 210–222.

978 Li, Y.X., Bralower, T.J., Montañez, I.P., Osleger, D.A., Arthur, M.A., Bice, D.M., Herbert, T.D., Erba, E., Premoli Silva, I., 2008.
979 Toward an orbital chronology for the early Aptian Oceanic Anoxic Event (OAE1a, 120 Ma). *Earth and Planetary*
980 *Science Letters* 271, 88–100.

981 Lorenzen, J., Kuhnt, W., Holbourn, A., Flögel, S., Moullade, M., Tronchetti, G., 2013. A new sediment core from the
982 Bedoulian (Lower Aptian) stratotype at Roquefort-La Bédoule, SE France. *Cretaceous Research* 39, 6-16.

983 Luciani, V., Cobianchi, M., Jenkyns, H.C., 2001. Biotic and geochemical response to anoxic events: the Aptian pelagic
984 succession of the Gargano Promontory (southern Italy). *Geological Magazine* 138, 277–298.

985 Mackenzie, A.S., Patience, R.L., Maxwell, J.R., Vandenbroucke, M., Durand, B., 1980. Molecular parameters of maturation
986 in the Toarcian shales, Paris Basin, France—I. Changes in the configurations of acyclic isoprenoid alkanes, steranes
987 and triterpanes. *Geochimica et Cosmochimica Acta* 44, 1709–1721.

988 Malinverno, A., Erba, E., Herbert, T.D., 2010. Orbital tuning as an inverse problem: chronology of the early Aptian oceanic
989 anoxic event 1a (Selli Level) in the Cismon APTICORE. *Paleoceanography* 25, PA2203.
990 <https://doi.org/10.1029/2009PA001769>

991 Martín-Chivelet, J., Berasategui, X., Rosales, I., Vilas, L., Vera, J.A., Caus, E., Gráfe, K.U., Mas, R., Puig, C., Segura, M., Robles,
992 S., Floquet, M., Quesada, S., Ruiz-Ortiz, P.A., Frenegal-Martínez, M.A., Salas, R., García, A., Martín-Algarra, A., Arias,
993 C., Meléndez, M., Chacón, B., Molina, J.M., Sanz, J.L., Castro, J.M., García-Hernández, M., Carenas, B., García-

- 994 Hidalgo, J., Gil J., Ortega, F., 2002. Cretaceous, in: Gibbons, W. and Moreno, T. (Eds.), *The Geology of Spain*. The
995 Geological Society, London, pp. 255–292.
- 996 Martínez-Ruiz, F., Kastner, M., Gallego-Torres, D., Rodrigo-Gámiz, M., Niero-Moreno, V., Ortega-Huertas, M., 2015.
997 Paleoclimate and paleoceanography over the past 20,000 yr in the Mediterranean Sea Basins as indicated by
998 sediment elemental proxies. *Quaternary Science Reviews* 107, 25–46.
- 999 Martínez-Ruiz, F., Paytan, A., Gonzalez-Muñoz, M.T., Jroundi, F., Abad, M.M., Lam, P.J., Bishop, J.K.B., Horner, T.J., Morton,
1000 P.L., Kastner, M., 2019. Barite formation in the ocean: Origin of amorphous and crystalline precipitates. *Chemical*
1001 *Geology* 511, 441-451. <https://doi.org/10.1016/j.chemgeo.2018.09.011>
- 1002 Marynowski, L., Zaton, M., Rakocinski, M., Filipiak, P., Kurkiewicz, S., Pearce, T.J., 2012. Deciphering the upper Famennian
1003 Hangenberg Black Shale depositional environments based on multi-proxy record. *Palaeogeography,*
1004 *Palaeoclimatology, Palaeoecology* 346, 66–86.
- 1005 Masse, J.P., Bellion, Y., Benkhelil, J., Boulin, J., Cornee, J.J., Dercourt, J., Guiraud, R., Mascle, G., Poisson, A., Ricou, L.E.,
1006 Sandulescu, M., 1993. Lower Aptian palaeoenvironments 114–112 Ma. In: Dercourt, J., et al. (Eds.), *Atlas Tethys*
1007 *Palaeoenvironmental Maps, Maps Beceip-Franlab, Rueil-Malmaison*.
- 1008 Méhay, S., Keller, C.E., Bernasconi, S.M., Weissert, H., Erba, E., Bottini, C., Hochuli, P.A., 2009. A volcanic CO₂ pulse triggered
1009 the Cretaceous Oceanic Anoxic Event 1a and a biocalcification crisis. *Geology* 37, 819–822.
- 1010 Menegatti, A.P., Weissert, H., Brown, R.S., Tyson, R.V., Farrimond, P., Strasser, A., Caron, M., 1998. High-resolution $\delta^{13}\text{C}$
1011 stratigraphy through the Early Aptian "Livello Selli" of the Alpine Tethys. *Paleoceanography* 13, 530–545.
- 1012 Millán, M.I., Weissert, H., Fernández-Mendiola, P.A., García-Mondéjar, J., 2009. Impact of Early Aptian carbon cycle
1013 perturbations on evolution of a marine shelf system in the Basque-Cantabrian Basin (Aralar, N Spain). *Earth Planet.*
1014 *Sci. Lett.* 287, 392–401.
- 1015 Millán, M.I., Weissert, H.J., López-Horgue, M.A., 2014. Expression of the late Aptian cold snaps and the OAE1b in a highly
1016 subsiding carbonate platform (Aralar, northern Spain). *Palaeogeography, Palaeoclimatology, Palaeoecology*, 167–
1017 179.
- 1018 Millán, M.I., Weissert, H.J., Owen, H., Fernández-Mendiola, P.A., and García-Mondéjar, J., 2011. The Madotz Urgonian
1019 platform (Aralar, northern Spain): Paleocological changes in response to Early Aptian global environmental
1020 events. *Palaeogeography, Palaeoclimatology, Palaeoecology* 312, 167–180.

- 1021 Moldovan, J.M., Seifert, W.K., Gallegos, E.J., 1985. Relationship between petroleum composition and depositional
1022 environment of petroleum source rocks. *American Association of Petroleum Geologists Bulletin* 69, 1255–1268.
- 1023 Molina, J.M., 1987. Análisis de facies del Mesozoico en el Subbético Externo. (Prov. de Córdoba y sur de Jaén). PhD thesis,
1024 Universidad de Granada, Granada, 512 pp.
- 1025 Molina, J.M., Hernández-Molina, F.J., 1993. Concreciones de barita en el Cretácico (Aptiense–Albiense) del Subbético
1026 (Cordilleras Béticas). *Boletín Geológico y Minero* 104, 548–573.
- 1027 Monteiro, F.M., Pancost, R.D., Ridgwell, A., Donnadieu, Y. 2012. Nutrients as the dominant control on the spread of anoxia
1028 and euxinia across the Cenomanian-Turonian oceanic anoxic event (OAE2): Model-data comparison.
1029 *Paleoceanography*, 27, art. no. PA4209. DOI: 10.1029/2012PA002351
- 1030 Moreno-Bedmar, J.A., Company, M., Sandoval, J., Tavera, J.M., Bover-Arnal, T., Salas, R., Delanoy, G., Maurrasse, F.J.M.R.,
1031 Martínez, R., 2012. Lower Aptian ammonite and carbon isotope stratigraphy in the eastern Prebetic Domain (Betic
1032 Cordillera, southeastern Spain). *Geologica Acta* 10, 333–350.
- 1033 Moullade, M., Tronchetti, G., Granier, B., Bornemann, A., Kuhnt, W., Lorenzen, J., 2015. High-resolution integrated
1034 stratigraphy of the OAE1a and enclosing strata from core drillings in the Bedoulian stratotype (Roquefort-La
1035 Bédoule, SE France). *Cretaceous Research* 56, 119–140.
- 1036 Mutterlose, J., Bottini, C., 2013. Early Cretaceous chalks from the North Sea giving evidence for global change. *Nature*
1037 *Communications*. <https://doi.org/10.1038/ncomms2698>
- 1038 Mutterlose, J., Bottini, C., Schouten, S., Sinninghe-Damsté, J.S., 2014. High sea-surface temperatures during the early
1039 Aptian Oceanic Anoxic Event 1a in the Boreal Realm. *Geology* 42, 439-442.
- 1040 Naafs, B.D.A., Castro, J.M., De Gea, G.A., Quijano, M.L., Schmidt, D.N., and Pancost, R.D., 2016, Gradual and sustained
1041 carbon dioxide release during Aptian Oceanic Anoxic Event 1a: *Nature Geoscience*. doi: 10.1038/ngeo2627.
- 1042 Naafs, B.D.A., Pancost, R.D., 2016. Sea-surface temperature evolution across Aptian Oceanic Anoxic Event 1a. *Geology* 44.
1043 <https://doi.org/10.1130/G38575.1>
- 1044 Najarro, M., Rosales, I., Moreno-Bedmar, J.A., Gea, G.A. de Barrón, E., Company, M., Delanoy, G., 2011. High-resolution
1045 chemo- and biostratigraphic records of the Early Aptian oceanic anoxic event in Cantabria (N Spain):
1046 Palaeoceanographic and palaeoclimatic implications. *Palaeogeography, Palaeoclimatology, Palaeoecology* 299,
1047 137–158.
- 1048 Newman, D.K., Neubauer, J., Ricci, J.N., Wu, C.H., Pearson, A., 2016. Cellular and Molecular Biological Approaches to
1049 Interpreting Ancient Biomarkers. *Annual Review of Earth and Planetary Sciences* 44, 493–522-

- 1050 Niebuhr, B., 2005. Geochemistry and time-series analyses of orbitally forced Upper Cretaceous marlimestone rhythmites
1051 (Lehrte West Syncline, northern Germany). *Geological Magazine* 142, 31-55.
- 1052 Nijenhuis, I.A., Becker, J., De Lange, G.J., 2001. Geochemistry of coeval marine sediments in Mediterranean ODP cores and
1053 a land section: implications for sapropel formation models. *Palaeogeography, Palaeoclimatology, Palaeoecology*
1054 165, 97-112.
- 1055 Nuñez-Useche, F., Barragán, R., Moreno-Bedmar, J.A., Canet, C., 2015. Geochemical and paleoenvironmental record of the
1056 early to early late Aptian major episodes of accelerated change: Evidence from Sierra del Rosario, Northeast
1057 Mexico. *Sedimentary Geology* 324, 47–66.
- 1058 O'Dogherty, L., 1994. Biochronology and Paleontology of mid-Cretaceous radiolarians from northern Apennines (Italy) and
1059 Betic Cordillera (Spain). PhD thesis, Institut de Géologie et Paléontologie, University of Lausanne, 413 pp.
- 1060 O'Dogherty, L., Aguado, R., de Gea, G.A., Sandoval, J., 2011. Registro isotópico del evento anóxico oceánico del Aptiense
1061 Inferior (OAE1a) en radiolaritas del Subbético. *Paleontologia i Evolució Memòria especial* 5, 273–275.
- 1062 Olivet, J.M., 1996. La cinématique de la plaque ibérique. *Bulletin des Centres de Recherches Exploration-Production Elf-*
1063 *Aquitaine* 20, 131–195.
- 1064 Ourisson, G., Albrecht, P., Rohmer, M., 1982. Predictive microbial biochemistry from molecular fossils to prokaryotic
1065 membranes. *Trends in Biochemical Sciences* 7, 236–239.
- 1066 Paschal, O., Carmichael, S.K., Königshof, P., Waters, J.A., Ta, P.H. Komatsu, T., Dombrowski, A., 2019. The Devonian-
1067 Carboniferous boundary in Vietnam: Sustained ocean anoxia with a volcanic trigger for the Hangenberg Crisis?.
1068 *Global and Planetary Change* 175, 64–81. <https://doi.org/10.1016/j.gloplacha.2019.01.02>
- 1069 Pedersen, T.F., Calvert, S.E., 1990. Anoxia vs. productivity: what controls the formation of organic-carbon-rich sediments
1070 and sedimentary rocks. *American Association of Petroleum Geologists Bulletin* 74, 454–466.
- 1071 Peters, K.E., Moldowan, J.M., 1991. Effects of source, thermal maturity, and biodegradation on the distribution and
1072 isomerization of homohopanes in petroleum. *Organic Geochemistry* 17, 47–51.
- 1073 Peters, K.E., Walters, C.C., Moldowan, J.M., 2005. 2nd ed. *The Biomarker Guide*. Cambridge University Press (1155pp.).
- 1074 Polteau, S., Hendriks, B.W.H., Planke, S., Ganerød, M., Corfu, F., Faleide, J.I., Midtkandal, I., Svensen, H.S., Myklebust, R.,
1075 2016. The Early Cretaceous Barents Sea Sill Complex: Distribution, $^{40}\text{Ar}/^{39}\text{Ar}$ geochronology, and implications for
1076 carbon gas formation. *Palaeogeography, Palaeoclimatology, Palaeoecology* 441, 83-95. [https://doi.org/](https://doi.org/10.1016/j.palaeo.2015.07.007)
1077 [10.1016/j.palaeo.2015.07.007](https://doi.org/10.1016/j.palaeo.2015.07.007)

- 1078 Price, G.D., 2003. New constraints upon isotope variation during the early Cretaceous (Barremian–Cenomanian) from the
1079 Pacific Ocean. *Geological Magazine* 140, 513–522.
- 1080 Quijano, M.L., Castro, J.M., Pancost, R.D., Gea, G.A. de, Najarro, M., Aguado, R., Rosales, I., Martín-Chivelet, J., 2012.
1081 Organic geochemistry, stable isotopes, and facies analysis of the Early Aptian OAE – New records from Spain
1082 (Western Tethys). *Palaeogeography, Palaeoclimatology, Palaeoecology* 365-366, 276–293.
- 1083 Rashby, S.E., Sessions, A.L., Summons, R.E., Newman, D.K., 2007. Biosynthesis of 2-methylbacteriohopanepolyols by an
1084 anoxygenic phototroph. *PNAS* 104:15099–104.
- 1085 Redfield, A.C., 1958. The biological control of chemical factors in the environment. *American Scientist* 46, 205–221.
- 1086 Renard, M., Rafélis, M., de Emmanuel, L., Moullade, M., Masse, J.P., Kuhnt, W., Bergren, J.A., Tronchetti, G., 2005. Early
1087 Aptian $\delta^{13}\text{C}$ and manganese anomalies from the historical Cassis-La-Bédoule stratotype sections (S.E. France):
1088 relationship with methane hydrate dissociation event and stratigraphic implications. *Carnets de Géologie* 1 (8)
1089 (Brest, Article 2005/04 (CG2005_A04)).
- 1090 Ricci, J.N., Morton, R., Kulkarni, G., Summers, M.L., Newman, D.K., 2016. Hopanoids play a role in stress tolerance and
1091 nutrient storage in the cyanobacterium *Nostoc punctiforme*. *Geobiology*, 15 (1), pp. 173-183.
1092 <https://doi.org/10.1111/gbi.12204>
- 1093 Robinson, S.A., Heimhofer, U., Hesselbo, S.P., Petrizzo, M.R., 2017. Mesozoic climates and oceans – a tribute to Hugh
1094 Jenkyns and Helmut Weissert. *Sedimentology* 64, 1-15, doi: 10.1111/sed.12349
- 1095 Robinson, S.A., Williams, T., Bown, P.R. 2004. Fluctuations in biosiliceous production and the generation of Early Cretaceous
1096 oceanic anoxic events in the Pacific Ocean (Shatsky Rise, Ocean Drilling Program Leg 198). *Paleoceanography*, 1-
1097 19. <https://doi.org/10.1029/2004PA001010>
- 1098 Roth, P.H., 1978. Cretaceous nannoplankton biostratigraphy and oceanography of the northwestern Atlantic ocean. Initial
1099 Reports of the Deep Sea Drilling Project 44, 731–759.
- 1100 Ruiz-Ortiz, P.A., 1980. Análisis de facies del Mesozoico de las Unidades Intermedias (entre Castril—provincia de Granada—
1101 y Jaén). Ph.D. Thesis. University of Granada, 372 pp.
- 1102 Ruiz-Ortiz, P.A., Molina, J.M., Nieto, L.M., Castro, J.M., de Gea, G., 2001. Itinerarios geológicos por el Mesozoico de la
1103 provincia de Jaén. 1. Introducción al Mesozoico de la parte externa del paleomargen sudibérico. Cordillera Bética:
1104 IV Coloquio del Cretácico de España, University of Jaén, pp. 11–24.

- 1105 Sánchez-Hernández, Y., Maurrasse, F., 2016. The influence of regional factors in the expression of oceanic anoxic event 1a
1106 (OAE1a) in the semi-restricted Organyà Basin, south-central Pyrenees, Spain. *Palaeogeography,*
1107 *Palaeoclimatology, Palaeoecology* 441, 582–598.
- 1108 Sanz de Galdeano, C., 1973. *Geología de la transversal Jaén-Frailes*. PhD thesis, Universidad de Granada, Granada, 274 pp.
- 1109 Schlanger, S.O., Jenkyns, H.C., 1976. Cretaceous oceanic anoxic events: causes and consequences. *Geologie en Mijnbouw*
1110 55, 179–184.
- 1111 Schoepfer, S.D., Shen, J. Wei, H., Tyson, R.V., Ingall, E., Algeo, T.J., 2015. Total organic carbon, organic phosphorus, and
1112 biogenic barium fluxes as proxies for paleomarine productivity. *Earth Science Reviews* 149, 19-48.
- 1113 Seifert, W.K., Moldowan, J.M., 1980. The effect of thermal stress on source-rock quality as measured by hopane
1114 stereochemistry. *Physics and Chemistry of the Earth* 12, 229–237.
- 1115 Sinningh -Damst , J.P., Kenig, F., Koopmans, M.P., Koster, J.G., Schouten, S., Hayes, J.M., De Leeuw, J.W., 1995. Evidence
1116 for gammacerane as an indicator of water column stratification. *Geochimica et Cosmochimica Acta* 59, 1895–
1117 1900.
- 1118 Skelton, P.W. (Ed.), 2003. *The Cretaceous World*. The Open University, Milton Keynes, and Cambridge University Press,
1119 Cambridge (360pp.).
- 1120 Skelton, P.W., Castro, J.M., Ruiz-Ortiz, P.A. 2019. Aptian carbonate platform development in the Southern Iberian
1121 Palaeomargin (Prebetic of Alicante, SE Spain). *BSGF – Earth Sciences Bulletin* 190 (2019) 3.
1122 <https://doi.org/10.1051/bsgf/2019001>
- 1123 Stein, M., F llmi, K.B., Westermann, S., Godet, A., Adatte, T., Matera, V., Fleitmann, D., Berner, Z., 2011. Progressive
1124 palaeoenvironmental change during the Late Barremian–Early Aptian as prelude to Oceanic Anoxic Event 1a:
1125 Evidence from the Gorgo a Cerbara section (Umbria-Marche basin, central Italy). *Palaeogeography,*
1126 *Palaeoclimatology, Palaeoecology* 302, 396–406.
- 1127 Stein, M., Westermann, S., Adatte, T., Matera, V., Fleitmann, D., Spangenberg, J.E., F llmi, K.B. 2012. Late Barremian-Early
1128 Aptian palaeoenvironmental change: The Cassis-La B doule section, southeast France. *Cretaceous Research*, 37,
1129 209-222. <https://doi.org/10.1016/j.cretres.2012.03.021>
- 1130 Summons, R. E., Jahnke, L. L., Hope, J. M., Logan, G. A., 1999. 2-Methylhopanoids as biomarkers for cyanobacterial oxygenic
1131 photosynthesis. *Nature* 400, 554– 557.

- 1132 Tejada, M.L., Suzuki, K., Kuroda, J., Coccioni, R., Mahoney, J.J., Ohkouchi, N., Sakamoto, N., Tatsumi, Y., 2009. Ontong Java
1133 Plateau eruption as a trigger for the early Aptian oceanic anoxic event. *Geology* 37, 855–858.
- 1134 Tribouillard N., Algeo T. J., Lyons T. W., Riboulleau A., 2006. Trace metals as paleoredox and paleoproductivity proxies: an
1135 update. *Chemical Geology* 232, 12–32.
- 1136 Turgeon, S.C., Brumsack, H.J., 2006. Anoxic vs dysoxic events reflected in sediment geochemistry during the Cenomanian-
1137 Turonian Boundary Event (Cretaceous) in the Umbria-Marche Basin of central Italy. *Chemical Geology* 234, 321-
1138 339.
- 1139 Tyson, R.V., 2001. Sedimentation rate, dilution, preservation, and total organic carbon: some results of a modeling study.
1140 *Organic Geochemistry* 32, 333–339.
- 1141 Tyson, R.V., 2005. The “productivity versus preservation” controversy; cause, flaws, and resolution. In: Harris, N.B. (Ed.),
1142 Deposition of Organic-carbon-rich Sediments Models, Mechanisms, and Consequences. Society for Sedimentary
1143 Geology (SEPM- SSG) Special Publication 82, pp. 17–33.
- 1144 van Breugel, Y., Schouten, S., Tsikos, H., Erba, E., Price, G.D., Sinninghe Damsté, J.S., 2007. Synchronous negative carbon
1145 isotope shifts in marine and terrestrial biomarkers at the onset of the early Aptian oceanic anoxic event 1a:
1146 Evidence for the release of ¹³C-depleted carbon into the atmosphere. *Paleoceanography* 22, PA1210. doi:
1147 10.1029/2006pa001341.
- 1148 Vera, J.A., 1988. Evolución de los sistemas de depósito en el margen ibérico de la Cordillera Bética. *Revista Sociedad*
1149 *Geológica España* 1, 373–391.
- 1150 Vera, J.A., 2004. Cordillera Bética y Baleares. In: Vera, J.A. (Ed.), *Geología de España*. Sociedad Geológica de España e
1151 Instituto Geológico y Minero de España, Madrid, pp. 345–464.
- 1152 Vergès, J., García-Senz, J., 2001. Mesozoic evolution and Cainozoic inversion of the Pyrenean Rift. In: Ziegler, P.A., Cavazza,
1153 W., Robertson, A.H.F., Crasquin-Soleau, J. (Eds.), *Peri-Tethys Memoir 6: Peri-Tethyan Rift/Wrench Basins and*
1154 *Passive Margins: Mémoires du Muséum National d'Historie Naturelle, Paris, 186, pp. 187–212.*
- 1155 Vilas, L., Martín-Chivelet, J., Arias, C., 2003. Integration of subsidence and sequence stratigraphic analyses in the Cretaceous
1156 carbonate platforms of the Prebetic (Jumilla-Yecla Region), Spain. *Palaeogeography Palaeoclimatology*
1157 *Palaeoecology* 200, 107–129.
- 1158 Volkman, J. K., Barrett, S. M., Blackburn, S. I., Man- Sour, M. P., Sikes, E. L., Gelin, F., 1998. Microalgal biomarkers: a review
1159 of recent research developments. *Organic Geochemistry* 29, 1163–1179.

- 1160 Waples, D.W., Machihara, T., 1991. Biomarkers for geologists. American Association of Petroleum Geologists—Methods in
1161 Exploration Series, 9 (91pp.).
- 1162 Warning, B., Brumsack, H.J., 2000. Trace metal signatures of eastern Mediterranean sapropels. *Palaeogeography,*
1163 *Palaeoclimatology, Palaeoecology* 158, 293-309.
- 1164 Wedepohl, K.H., 1991. The composition of the upper Earth's crust and the natural cycles of selected metals. Metals in
1165 natural raw materials. Natural resources. In: Merian, E. (Ed.), *Metals and Their Compounds in the Environment.*
1166 VCH, Weinheim, pp. 3–17.
- 1167 Weissert, H., 1990. Siliciclastics in the Early Cretaceous Tethys and North Atlantic oceans: documents of periodic
1168 greenhouse climate conditions. *Mem. Soc. Geol. Ital.* 44, 59–69.
- 1169 Weissert, H., Erba, E., 2004. Volcanism, CO₂ and palaeoclimate: a Late Jurassic–Early Cretaceous carbon and oxygen isotope
1170 record. *Journal of the Geological Society, London* 161, 1–8.
- 1171 Welander, P.V., Coleman, M.L., Sessions, A.L., Summons, R.E., Newman, D.K., 2010. Identification of a methylase required
1172 for 2-methylhopanoid production and implications for the interpretation of sedimentary hopanes. *Proceedings of*
1173 *the National Academy of Sciences* 107, 8537-8542. <https://doi.org/10.1073/pnas.0912949107>
- 1174 Westermann, S., Föllmi, K.B., Adatte, T., Matera, V., Schnyder, J., Fleitmann, D., Fiet, N., Ploch, I., Duchamp-Alphonse, S.,
1175 2010. The Valanginian d¹³C excursion may not be an expression of a global anoxic event. *Earth and Planetary*
1176 *Science Letters* 290, 118-131.
- 1177 Westermann, S., Stein, M., Matera, V., Fiet, N., Fleitmann, D., Adatte, T., Föllmi, K.B., 2013. Rapid changes in the redox
1178 conditions of the western Tethys Ocean during the early Aptian oceanic anoxic event: *Geochimica et*
1179 *Cosmochimica Acta* 121, 467–486.
- 1180 Westermann, S., Vance, D., Cameron, V., Archer, C., Robinson, S.A., 2014. Heterogeneous oxygenation states in the Atlantic
1181 and Tethys oceans during Oceanic Anoxic Event 2. *Earth and Planetary Science Letters* 404, 178-189.
1182 <https://doi.org/10.1016/j.epsl.2014.07.018>
- 1183 Xie, S., Pancost, R.D., Yin, H., Wang, H., Evershed, R.P. 2005. Two episodes of microbial change coupled with Permo/Triassic
1184 faunal mass extinction. *Nature*, 434, 494-497. <https://doi.org/10.1038/nature03396>
- 1185 Xu, W., Ruhl, M., Jenkyns, H.C., Hesselbo, S.P., Riding, J.B., Selby, D., Naafs, B.D.A., Weijers, J.W.H., Pancost, R.D., Tegelaar,
1186 E.W., Idiz, E.F., 2017. Carbon sequestration in an expanded lake system during the Toarcian oceanic anoxic event.
1187 *Nature Geoscience* 10, 129-134. <https://doi.org/10.1038/ngeo2871>

- 1188 Yamamoto, K., Ishibashi, M., Takayanagi, H., Asahara, Y., Sato, T., Nishi, H., Iryu, Y. 2013. Early Aptian paleoenvironmental
1189 evolution of the Bab Basin at the southern Neo-Tethys margin: Response to global carbon-cycle perturbations
1190 across Ocean Anoxic Event 1a. *Geochemistry, Geophysics, Geosystems*, 14, 1104-1130.
1191 <https://doi.org/10.1002/ggge.20083>
- 1192 Ziegler, P.A., 1988. Evolution of the Arctic–North Atlantic and the Western Tethys, publ. *Int. lithos. Program*, 0144. AAPG
1193 Memoir 43 (193pp.)